Development of Co-Assembly Methods for Improved Graphene/Ionic Liquid Supercapacitors

by

Zimin She

A thesis

presented to the University of Waterloo

in fulfilment of the

thesis requirement for the degree of

Master of Applied Science

in

Chemical Engineering (Nanotechnology)

Waterloo, Ontario, Canada, 2017

AUTHOR'S DECLARATION

I hereby declare that I am the sole author of this thesis. This is a true copy of the thesis, including any required final revisions, as accepted by my examiners.

I understand that my thesis may be made electronically available to the public.

ABSTRACT

Supercapacitors, also known as electric double-layer capacitors or ultracapacitors, store energy by rapid and reversible rearrangement of ions/charges at the electrolyte/electrode interface. This physical process results in various advantages, such as high power density and long lifespan. However, compared to batteries, supercapacitors still have significantly lower energy density. Currently, great efforts focus on pursuing the efficient combination of high specific surface area (SSA) electrodes and electrolytes with wide working voltage windows. Hence, graphene-based materials have attracted considerable interest due to their high electrical conductivity and theoretical SSA, they are promising candidates for electrochemical double-layer capacitors (EDLCs) as next-generation energy storage devices.

The objective of this work is to develop new electrode fabrication methods to improve the performance of reduced graphene oxide (rGO) based supercapacitors. Since specific capacitance is proportional to the SSA, the main challenge for rGO based supercapacitors is to effectively prevent rGO sheets from restacking when processed into a dense, thick electrode. In the first part, a hydrophobic ionic liquid (IL), 1-ethyl-3-methylimidazolum bis(trifluoromethyl-sulfonyl)imide (EMImTFSI), is used as both electrolyte and spacer to separate the graphene sheets and maintain its high SSA. It is demonstrated that EMImTFSI has better chemical stability than 1-ethyl-3-methylimidazolium tetrafluoroborate ($EMImBF_4$), which was used in our previous work, and reduces the corrosion of commonly used current collectors (e.g. Al, Cu). To imbibe IL prior to thermal reduction, a graphene oxide/IL dispersion was used to assembly gel-

like laminated nanocomposite on common metal current collectors. To balance the loss of IL and the reduction of GO, GO/IL electrodes were reduced by ramping up from room temperature to 360 ºC at 5 ºC/min followed by rapid cooling. The resulting conductive films containing 80 wt% of EMImTFSI displayed a good gravimetric capacitance of 135 F/g at 5 mV/s.

The above work did not take advantage of any specific interactions between the IL and GO and thus some restacking likely occurred and limited the IL-accessible surface area. Therefore, the second half of this thesis focuses on engineering specific interactions between the GO and EMImTFSI to enable a more uniform distribution of IL among the network of GO sheets. This was achieved through an EMImTFSI aqueous microemulsion formed by the addition of the surfactant, Tween 20. Under a water rich condition (> 70 wt% water), this system became an IL-in-water microemulsion and displayed an average surfactant-stabilized IL droplet size of ~8 nm. In order to observe the interaction between microemusion nanodroplets and GO sheets, the fluorescence response arising from Tween 20 and rhodamine-b were used to probe adsorption through fluorescence quenching. A significant decrease in fluorescence intensity in the presence of GO indicated the spontaneous adsorption of stabilized IL onto the GO surface – likely via hydrogen bonding. Finally, this GO dispersion with uniformly adsorbed IL-containing microemulsion nanodroples was drop-casted onto Cu foil. The precursor electrode was reduced at 300 °C to release IL and remove Tween 20 leading to a dense and conductive layered rGO/IL film (0.76 g/cm^3 of rGO), which exhibited record high gravimetric

(302 F/g) and volumetric capacitance (218 F/cm^3). These results constitute the best performance of a graphene-based high voltage supercapacitor reported to date.

ACKNOWLEDGEMENTS

I would first like to thank my supervisor Dr. Michael A. Pope for guiding me through my Master's studies. His patience, motivation and enthusiasm to research have had a big impact on my studies. I deeply appreciate his guidance and patience while I was writing my thesis, in addition to helping my written English. I would also like to thank Dr. Aiping Yu and Dr. Jeff Gostick for being on my committee. I would again like to thank Dr. Linda Nazar for letting me use her X-ray diffraction system as well as Dr. Juewen Liu for letting me use his Zetasizer instrument. I would also like to thank Dr. Debasis Ghosh for his contributions in our collaborations. Last but not least, I would like to thank my lab mates and my friends for their support throughout my masters.

Finally, I would like to thank my parents for their unwavering support while I'm pursuing my graduate studies in Canada.

DEDICATION

Dedicated to my Family

TABLE OF CONTENTS

LIST OF FIGURES

LIST OF TABLES

LIST OF ABBREVIATIONS

GO	Graphene oxide
rGO	Reduced graphene oxide
EDLCs	Electric double-layer capacitors
RTILs	Room temperature ionic liquids
FGS	Functionalized graphene sheets
SSA	Specific surface area
DI water	Deionized water
EMImTFSI	1-ethyl-3-methylimidazolum bis(trifluoromethylsulfonyl)imide
$EMImBF_4$	1-ethyl-3-methylimidazolium tetrafluoroborate
DMF	Dimethylformamide
UV	Ultraviolet rays
2D	2-dimensional
SEM	Scanning electron microscopy
XRD	X-Ray powder diffraction
TGA	Thermogravimetric analysis

1 Introduction

Supercapacitors, which are also known as ultracapacitors or electric double layer capacitors (EDLCs), store energy by forming an electric double layer through fast and highly reversible charge/ion rearrangement at the electrode/electrolyte interface, primarily using high specific surface area (SSA) electrode materials such as activated carbons and, more recently, graphene.[1-3] The physical, as opposed to chemical, energy storage mechanism is responsible for the exceptional cycle life and fast charge/discharge capabilities of these devices. The high SSA and thin capacitive double-layer that forms between the electronic and ionic charge leads to a capacitance which is many orders of magnitude larger than traditional dielectric and electrolytic capacitors.

Primary energy sources exist in various forms, including the combustion of fossil fuels, nuclear energy and renewable energy like hydropower and wind. According to statistics about world energy consumption from 1988 to 2013, fossil fuels are still the leading energy source, with 32.9% of global energy consumption.[4] However, limited reserves, significant carbon dioxide emissions and other pollutants are impacting global warming and human health. Hence, the need to reduce CO_2 and other greenhouse gas emissions has become a topic of great importance. Such emissions are the epitome of the

energy and environmental crises, and thus, developing advanced green energy storage systems to better manage electrical energy (e.g. supercapacitors, batteries, fuel cells, etc.) is of extreme urgency.[5-6] Compared to other energy storage systems, supercapacitors have many practical advantages. Due to the physical nature of the charge storage process, supercapacitors can be used over a wider range of voltages and temperatures compared to lithium-ion batteries. The improved safety and cycle life greatly decreases maintenance costs and promotes working reliability. At the present time, EDLCs are mainly used in the following fields:[6-7]

1. *Transportation*: Supercapacitors have been widely used as the auxiliary power source in electric vehicles, such as cars, trucks and trains. Presently, electric vehicles use lead-acid batteries as main power supply. Apart from the high cost for battery replacement, another critical problem for electric vehicles is the tremendous power consumption in starting the engine, which is especially high for heavy transportation (e.g. trucks and trains). Using supercapacitors as the power supply for the ignition system relieves the lead-acid batteries of harsh discharging, which significantly extends its lifespan. Meanwhile, supercapacitors can collect the regenerative energy from the braking process to further save running costs. Since lead is being banned by countries for environmental protection, supercapacitors-powered electric vehicles are under development in recent decades. In 2012, the China Railway Rolling Stock Corporation (CRRC) has built a light rail system using supercapacitors as the main power source. This supercapacitor-powered train can be fully charged during a 30 seconds stop and

run 3 to 5 kilometers at 70 km/h to the next stop. A total of 350 passengers can be held and 85 % of energy generated during braking is collected and returned to the energy storage system.

2. *Back-up Power*: Temporary back-up power is a common requirement for a wide range of applications whenever the main power source is suffering a sudden blackout. This highly reliable back-up system is mainly needed for data back-up applications ranging from servers to solid-state drives, power fail alarms in industrial or medical applications, and some other special fields, such as pitch control system in windmills. Compared to batteries, supercapacitors have better safety and longer cycle life, especially in demanding environments (e.g. low or high working temperature). Furthermore, supercapacitors can provide a burst of energy in a very short time. These advantages make supercapacitors an excellent choice for short term power back-up required in seconds or minutes. For example, windmills usually work under a significant diurnal temperature variation. Once it suffers a sudden main power failure, it needs a back-up power to return the turbine blades to a neutral position for safe shutdown.
3. *Consumer Electronics*: To meet the increasing requirement for smart and portable devices, supercapacitors have become the emerging energy storage technology used in consumer electronics, including laptops, digital cameras, portable speakers and mobile computing. Apart from the improved safety and charging efficiency, compared to rechargeable batteries, supercapacitors can effectively prevent products from over-sizing due to the size of the batteries in order to meet

their high power demands. For example, Blueshift designed the first supercapacitor-powered speakers in 2013, which has a more powerful sound playback than traditional portable speakers of the same size. Moreover, it only takes 5 minutes in charging to play at full volume for 6 hours while other battery-powered speakers take 3 hours for 15 hours of operation.

4. *Military and Aerospace:* Due to their excellent power density and low equivalent series resistance (ESR), supercapacitors are combined with high energy density batteries to form the pulsed power source usually used for laser weapons, radars and aircrafts.

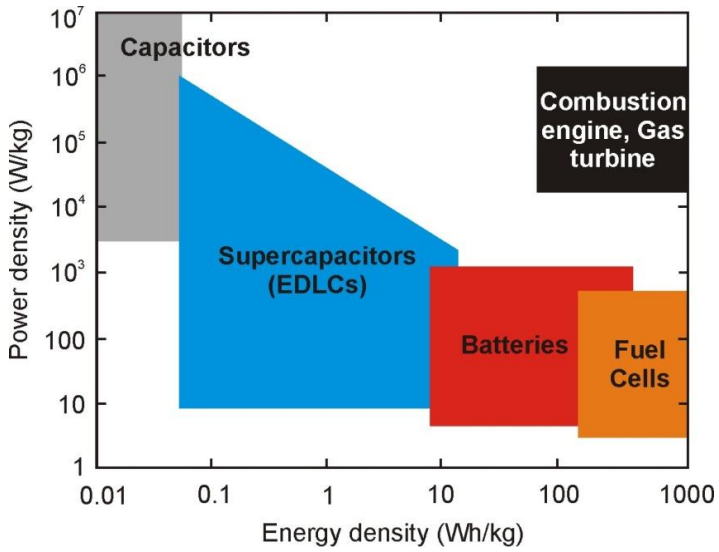

Figure 1.1: Ragone plot illustrating typical energy and power densities of portable energy storage devices. (Reproduced from ref. 5)

However, compared to other energy storage devices like batteries and fuel cells, supercapacitors still have significant lower energy density as shown in the **Figure 1.1.** The poor energy density is one of the main factors which restrict their commercial application, while another one is the high cost to performance ratio. Hence, major efforts

are underway to improve the energy density of supercapacitors based on simpler and more environmental friendly manufacturing processes while maintaining their unique advantages such as high power density, long cycle life and improved safety.

Before outlining detailed objectives of this work, the following section reviews the main classification of supercapacitors and general operating principle, the factors which affect their performance and the materials currently used as electrodes.

2 Background

2.1 Operation Principles of Supercapacitors

Supercapacitors are usually classified into two types based on the mechanism of energy storage:[8] EDLCs store energy only through a physical rearrangement of charges/ions while pseudocapacitors take advantage both electric double-layer (EDL) charging and highly reversible redox reactions which help boost the capacity but typically at the expense of reduced power and cycle-life.

2.1.1 Electric Double Layer Capacitors

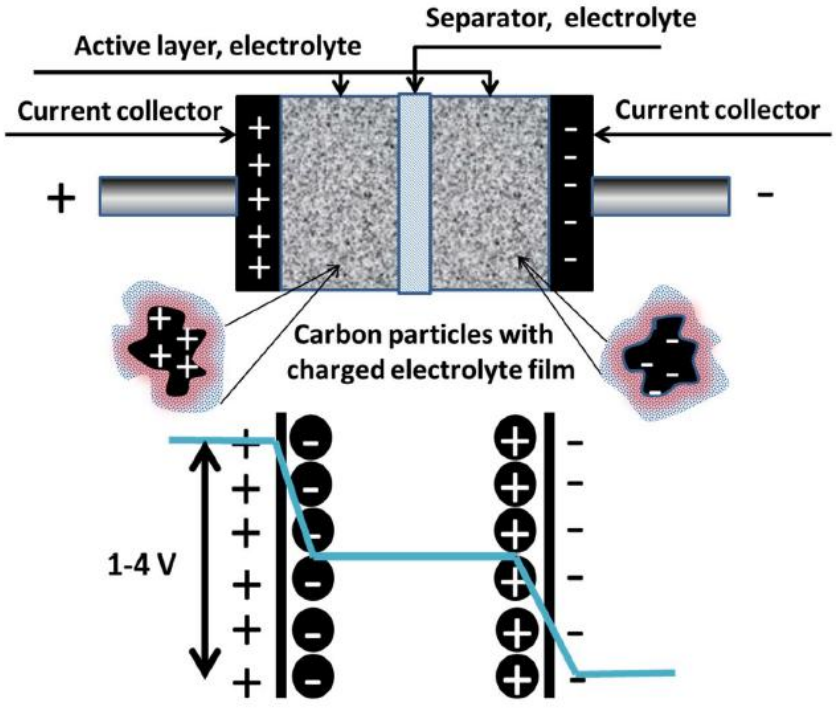

Figure 2.1: Schematic structure and principles of a single cell EDLC. (Reproduced from ref. 9)

As shown in Figure 2.1, a typical EDLC cell is composed of two current collectors, two electrodes (also called active layers), electrolyte and a separator which prevents the electrodes from contacting electrically but allows ions to pass. During the process of charging, electrons are pumped from the positive electrode to the negative electrode by a power supply. Meanwhile, due to the potential difference, cations in electrolyte travel to the negative electrode while anions move towards the positive electrode. The reverse process happens in the process of discharging.

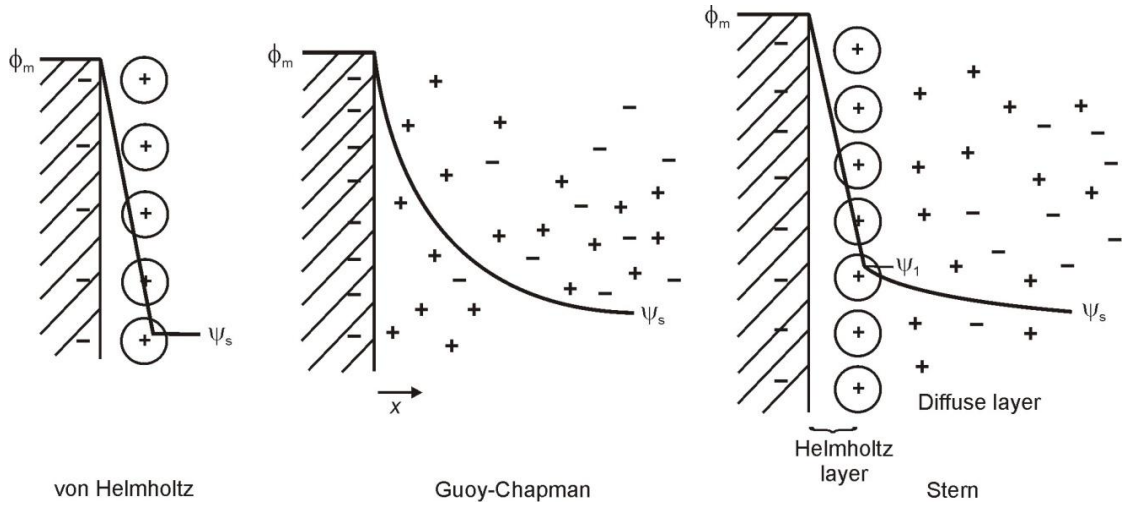

Figure 2.2: Different theoretical models for EDL: (a) Helmholtz model, (b) Guoy-Chapman model, (c) Stern model. (Reproduced from ref. 2)

The physical structure of the EDL proposed by Helmholtz consists of two parallel layers of closely spaced and oppositely charged electronic and ionic charges as shown in **Figure 2.2a**.[2] However, this simple model does not consider the thermal motion of ions and the more extended distribution of ions near the electrode/electrolyte interface that this causes. Another drawback is that this model cannot explain the experimentally measured dependence of capacitance on electrolyte concentration and applied potential. The thermal fluctuation and other factors were first incorporated into the EDL model by Gouy

and Chapman. Due to the thermal fluctuation tend,[10] ions near the electrode surface cannot remain static in a packed array as described by Helmholtz. Hence, these ions will redistribute to form the so-called diffuse layer following the Poisson-Boltzmann equation[11] resulting in the change of potential as a function of distance as shown in **Figure 2.2b**. This region is the so-called diffuse layer, having a net charge equal and opposite to the charge at the electrode site. The main problem for this model is that they considered ions in the electrolyte as point charges, causing the overestimation of capacitance. Without a size limitation, ions can get infinitely close to the surface of the electrode when it is highly charged. Hence, Stern came up with a modified model by combining the two previous models. As shown in **Figure 2.2c**, EDL is divided into two regions, the modified Helmholtz layer and the diffuse layer (used by Gouy and Chapmann) extending to the bulk solution. According to this model, the measured capacitance of EDL (C_{DL}) can be estimated by considering the capacitance of each of these layers in series:

$$\frac{1}{C_{\mathrm{DL}}} = \frac{1}{C_{\mathrm{Diff}}} + \frac{1}{C_{\mathrm{H}}}$$

where C_{Diff} and C_H is the capacitance contributed by the diffuse layer and Helmholtz layer, respectively. Since the two capacitances are added in series, the measured capacitance is mainly decided by the smaller one. As C_{Diff} is proportional to the root of electrolyte concentration, C_H will dominate the resulting measured capacitance at high electrolyte concentration (> 0.1 M). Since increasing the electrolyte concentration is easier to achieve, while C_H is typically constant for a given electrode and electrolyte, C_{DL} is usually estimated by:

$$C_{\mathrm{DL}} = \frac{Q}{U} = \frac{\varepsilon_{\mathrm{r}} \cdot \varepsilon_0}{d} \cdot A$$

where ε_{r} is the electrolyte dielectric constant, ε_0 is the vacuum dielectric constant, d is the distance of closest approach of an ion to the surface and A is specific sureface area of a single electrode. Generally, the capacitance (C) and operating voltage window (U) vary according to the type of electrolyte. For a given electrode material, a higher specific capacitance is typically observed in an aqueous electrolyte (such as H_2SO_4 or KOH) [12-13] than that in ionic liquid or organic electrolyte. This is typically ascribed to the smaller size of ions in aqueous electrolytes compared to that in other electrolytes, resulting in smaller distances of closest approach (d) and higher ions accessible SSA.[14] Also, pseudocapacitance is usually observed in aqueous electrolyte which adds to the capacitance by EDL. However, usually only 0.5 ~ 1 V of working voltage can be achieved in aqueous electrolyte due to the decomposition voltage of water (1.2 V) and stability of some active materials (like Mxenes, etc).[15] Even if the voltage limitation can be pushed to 2 V in aqueous electrolyte due to the overpotential for oxygen and hydrogen evolution in some electrolyte/material systems,[16] it is still much less than that of ionic liquid or organic based devices which can work stably at > 3V. The capacitance of the device (C) and working voltage window (U) mainly decide the resulting specific energy (E) and power density (P) of an EDLC, which are the most important criteria for evaluating their performance in comparison to other energy storage technologies and can be generally estimated by:

$$E = \frac{1}{2} C \cdot U^2$$

$$P = \frac{E}{t}$$

where t is the discharge time in galvanostatic charge/discharge plots at corresponding current density.

2.1.2 Pseudocapacitors

As discussed briefly above, another charge storage mechanism can add to the double-layer capacitance, namely the pseudocapacitance arising from reversible Faradaic reactions. Pseudocapacitors store energy mainly through underpotential deposition, chemical adsorption/desorption or highly reversible redox on the surface of active materials. Each of these mechanisms requires partial or complete transfer of electronic charge across the electrode/electrolyte interface via a quasi-reversible chemical reaction.[17] Based on this energy storage principle, pseudocapacitors store energy not only on the surface of electrodes but also in the interior of electrodes which suggests higher specific capacitance and energy density than that of EDLCs. The first device operating primarily by a pseudocapacitance mechanism was designed in 1971 which uses RuO_2 as the active material.[18-19] In the 1990s Conway's group provided the first detailed explanation for the operating principle of a pseudocapacitor operation by three different mechanisms[20] — (1) Underpotential Deposition: when a kind of substance A (typically, a metal cation which will be reduced onto another metal substrate) has stronger interaction with the substrate B than that with itself, the reduction of corresponding metal A ions can occur at a potential less negative than its equilibrium potential. As a classical case, a single layer of Pb particles could be adsorbed onto the surface of a Au substrate as plotted in Figure 2.3a; (2) Redox Pseudocapacitance: this mechanism relies on reversible

Faradic charge transfer which occurs when ions in electrolyte (most often protons) chemically react with the electrode material (Figure 2.3b); (3) Intercalation Pseudocapacitance: the third possible mechanism is known as intercalation pseudocapacitance. In this case, electrolyte ions can reversibly insert into the porous structure of the electrode material. This causes the material to become partially oxidized/reduced, producing a salt of the intercalated ion and typically a layered material such as graphite or MoS_2. Generally, there is no change to the crystal lattice of the insertion host. The basic mechanism is shown in **Figure 2.3c**.

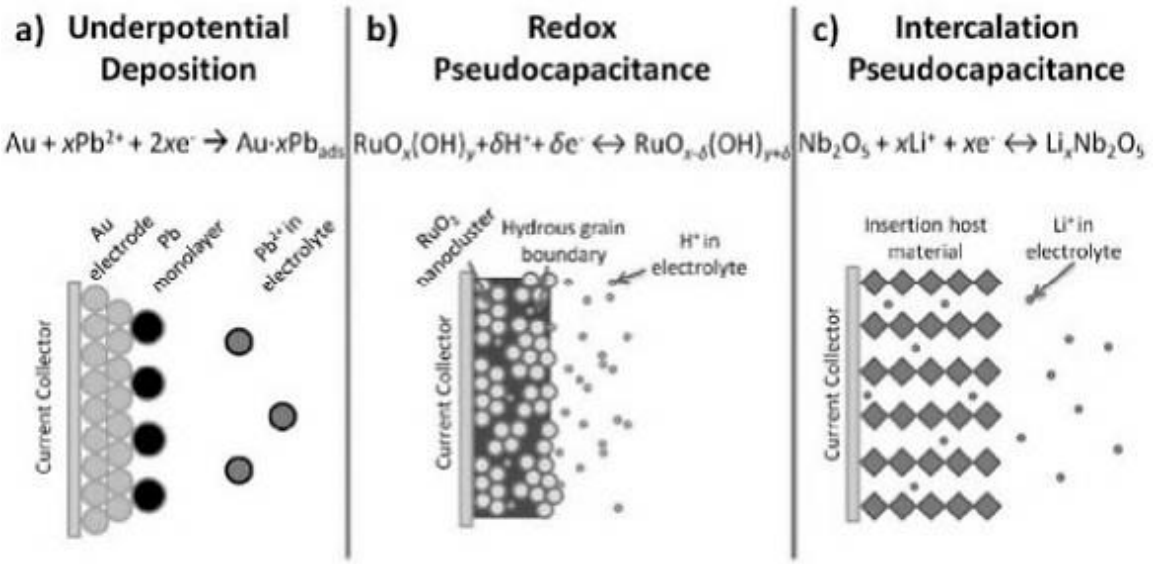

Figure 2.3: Different types of mechanisms to pseudocapacitors: (a) underpotential deposition, (b) redox pseudocapacitance, (c) intercalation pseudocapacitance. (Reproduced from ref. 20)

2.2 Electrode materials

The electrode material is one of the most important components of a supercapacitor. The choice of the material will dramatically influence the final electrochemical performance. Therefore, ongoing efforts attempting to boost the performance of supercapacitors mainly focus on designing new electrode materials. Carbonaceous

materials, metal oxides, conductive polymers and composites containing two or more of the above materials are the four major classes of promising materials being tested as the active layers in supercapacitors.

2.2.1 Carbonaceous Materials

The combination of various advantages, such as low cost and high SSA, implies a huge potential for carbonaceous materials to be used as electrodes in supercapacitors. The inherent corrosion resistance of carbonaceous materials allows them to be stable among a wide working voltage window and operated for millions of cycles with little performance degradation. Presently, various carbonaceous materials have been reported in EDLC-related literature, including carbon fibres, carbon aerogels, carbon blacks, activated carbons, carbon nanotubes and graphene based materials.[21-22] A more detailed review of graphene-based materials is given in Section 2.3 as this material and its use in EDLCs is the focus of this thesis work.

2.2.2 Metal Oxides

Metal oxides are a common active material for pseudocapacitors which store energy through fast and highly reversible chemical redox reactions between ions in electrolyte and active materials. Various metal oxides have been studied including MnO_2, Co_3O_4, NiO, RuO_2 and V_2O_5.[23-27] With their outstanding theoretical capacitance which is usually ten times greater than that of EDLCs (e.g. the theoretical gravimetric capacitance of MnO_2 is as high as ~ 1370 F/g),[28] noble metallic oxides are becoming more and more popular among researchers. However, the commercial application of metal oxides based supercapacitors are significantly restricted due to their poor cycle life, narrow voltage

window and high cost, so they are commonly composited together with carbon materials or other supporting materials so as to prevent structural collapse during cycling.

2.2.3 Conductive Polymers

Conductive polymers also belong to the pseudocapacitor active material family.[29-30] Polyaniline (PANI), polythiophene, polypyrrole (PPY) and other polymers with conjugated structure are mainly used as active materials in pseudocapacitors. These materials mainly store energy by fast reversible N-type or P-type doping/dedoping redox reactions on its surface, resulting in very high theoretical capacitance (e.g. PANI fibre can achieve a maximum capacitance of ~ 2000 F/g in 1 M H_2SO_4).[31] N-type doping (or so-called reductive doping) means that polymers obtain additional free electrons onto its molecular chains from an external circuit. These delocalized N-doping electrons make the polymer negatively charged and attract counterions from the electrolyte into its polymer matrix. Similarly, P-type doping (or called as oxidative doping) can be positively charged by losing free electrons from its polymer matrix during the charging process. However, long time charge/discharge cycling can cause volume shrinkage/expansion which leads to the collapse of the polymer structure, resulting in a very poor cycle life.

2.2.4 Composite Electrodes

Electrode materials composed of two or more active materials are referred to as composite electrodes. According to the number of composite components, they can be classified as binary compound electrodes (such as graphene/PANI), ternary electrodes (such as graphene/MnO_2/PANI) and so on.[32-33] Because composite electrodes can combine and remedy respective merits/demerits of different composite components, they have broad application potential and good development prospect.

2.3 Graphene based Materials

2.3.1 Structure and Properties of Graphene

In 2004, graphene was first discovered by Andre Geim and Konstantin Novoselov from Manchester University by mechanical exfoliation and immediately aroused world-wide interest, which led to them winning the Nobel Prize in 2010.[34] Graphene is a well-known 2D nanomaterial which is densely composed of a monolayer of sp^2 hybridized carbon atoms arranged in a hexagonal lattice (**Figure 2.4**), so it can be considered as an exfoliated single-layer graphite sheet. All sp^2 hybrized carbon atoms are connected with three adjacent atoms through very strong σ covalent bonding leading to it having a high modulus of elasticity (~1 TPa) and ultimate breaking strength (~130 GPa).[35] Moreover, each sp^2 hybrized carbon atom can contribute an unpaired p electron to form π bonds, whose electrons can quickly move among lattice network, resulting in a prominent conductivity. From the perspective of the geometric structure, graphene can be interpreted as the basic structural unit for other carbonaceous allotropes, including 0D fullerene, 1D CNT and 3D graphite.

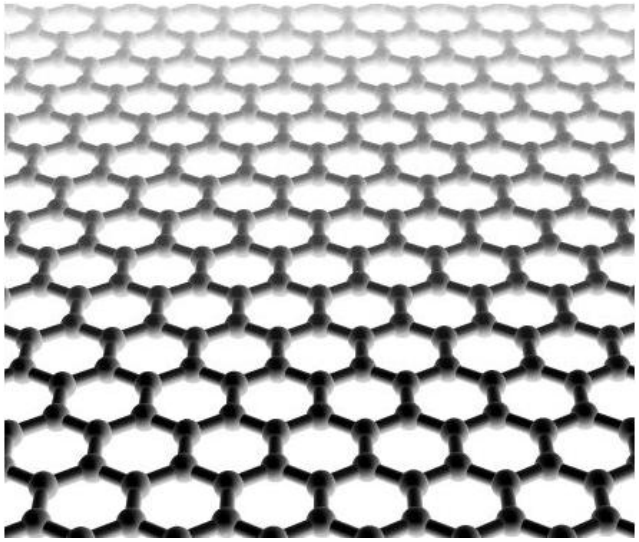

Figure 2.4: Three-dimension view of ideal graphene crystalline structure.

The unique structure makes graphene an advanced material possessing the combination of the nature of metals and nonmetals resulting in a number of distinguished advantages. It is considered as one of the most promising materials for next generation flexible films for use as electrodes in supercapacitors because (1) the two-dimensional structure can provide a large surface area (2600 m^2/g),[36] which serves as an extensive transport platform for associating with ions in electrolytes; (2) the high electrical mobility (can achieve as high as 20 m^2/Vs by minimizing impurity scattering)[37] of graphene sheets enables their great potential to be highly electrically conductive through electrical or chemical doping, therefore leading to enhanced power density and rate capability; and (3) the superior mechanical property allow graphene sheets to be easily assembled into free-standing films with robust mechanical stability. This graphene is also called pristine graphene which is defined as the single layer of graphite containing no functional group and few lattice defects. After pristine graphene was first prepared by cleaving a block of highly ordered pyrolytic graphite with Scotch tape, many other methods have been developed, such as chemical vapor deposition (CVD). However, these preparation methods for pristine graphene cannot yield large volumes of material economically and efficiently to be used for thick electrode films. In addition, the theoretical capacitance of pristine graphene is low (< 200 F/g) as it is limited by graphene's low electronic density of states (DOS).[38] Hence, many "modified pristine graphene" or graphene based materials have bene designed, especially the route based on the exfoliation of graphene oxide (GO) is widely applied.[39-40] The resulting product is referred to as reduced graphene oxide (rGO) or functionalized graphene sheets (FGSs), the theoretical specific capacitance of these materials is larger (~500 F/g) due to the introduction of lattice

defects and functional groups that increases the electronic DOS. More detailed review of research about this material is provided in next section.

2.3.2 Review of Graphene-Based EDLCs

Outstanding conductivity and super-high SSA enables rGO or FGSs to achieve a prominent theoretical specific capacitance as high as > 500 F/g, is the largest among all carbonaceous-based supercapacitors.[41] Furthermore, the stable chemical and physical properties of graphene lead to excellent cycling stability. In 2008, Stoller et al.[36] first demonstrated the use of chemically reduced graphene oxide as an electrode material in supercapacitor. The devices exhibited a capacitance of 135 F/g in 5.5 mol/L KOH, this value is far less than the theoretical specific capacitance. This large difference from the theoretical capacitance is mainly caused by the agglomeration and restacking of graphene sheets resulting from the interplanar pi-pi interaction and van der Waals forces, which can greatly reduce the surface areas and limit the ability of electrolyte ions to penetrate between graphene layers. To solve this core challenge of graphene-based EDLCs, many different methods have been reported in the past decade.

Separating the sheets by appropriate spacers is an effective approach to prevent the restacking of graphene sheets. The most widely investigated spacers are carbonaceous materials (e.g., carbon particles, CNT), metals (e.g., Pt, Au) or metal oxides (e.g., SnO_2), and other pseudocapacitive materials (e.g., transitional metal oxides, hydroxides and conducting polymers).

Samulski et al.[42] were the first to demonstrate this concept by decorating graphene sheets with Pt nanoparticles to physically prevent them from face-to-face restacking. This composite exhibited a high specific surface area of 862 m^2/g, which improved the

specific capacitance of dried pure graphene from 14 F/g to 269 F/g. Yan et al.[43] designed a fast synthetic method for graphene/MnO_2 composite through the self-limiting deposition of nano-scale MnO_2 on the surface of graphene under microwave radiation. This composite containing 78 wt% of MnO_2 exhibited a max capacitance of 310 F/g and remained 95.4 % of initial capacitance after 15000 cycles at 500 mV/s.

Due to the high capacitance, low cost and simple synthetic process compared to other conductive polymers (e.g. PPY, polythiophene), PANI is one of the most promising for a solid spacer in graphene based electrodes. Hao et al.[44] reported a new electrode material by mixing PANI with graphene, this fiber-like PANI was synthesized by in situ polymerization in the presence of graphene sheets. This composite displayed a capacitance of 531 F/g, which is much higher than the capacitance of pure PANI or pure graphene based supercapacitors suggesting a synergistic effect. Wei and Han et al. discussed a special composite structure where PANI nanowires vertically align on the surface of graphene oxide sheets. The unique structure and mechanical property of graphene oxide effectively prevent PANI from deforming during chemical redox resulting in improved cyclic stability.

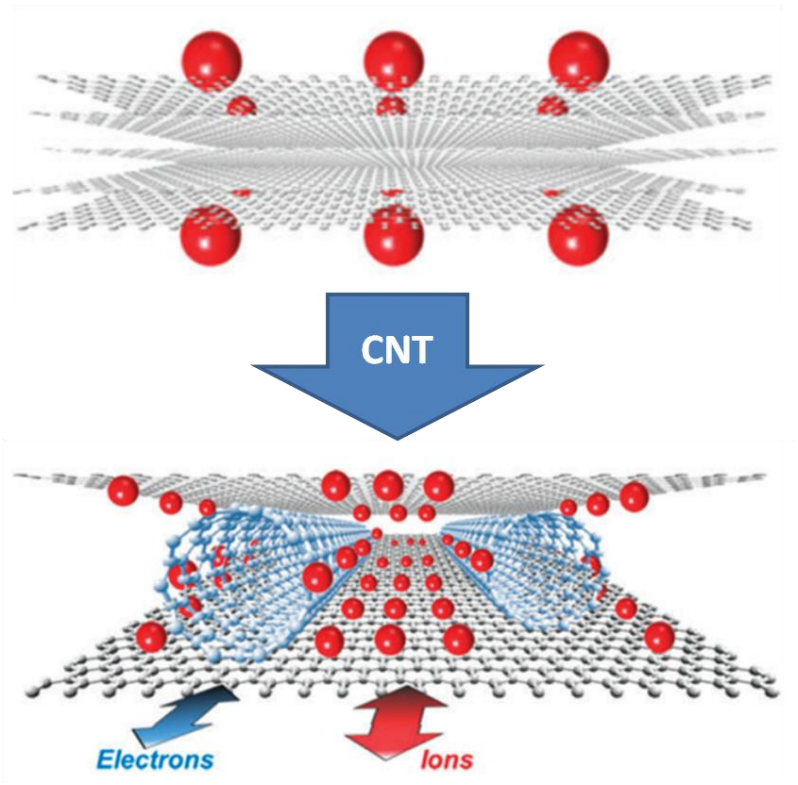

Figure 2.5: Structure of graphene based materials mixed with CNT.

CNT is also considered as the one of common spacers because of outstanding conductivity and high SSA. National Institute for Materials Science Japan (NIMS) found that CNT can be spontaneously intercalated into graphene sheets through self-assembly, which generate proper voids leading to increased density of current and ions. The modified electric conduction model after added CNT was plotted in **Figure 2.5**. The resulting CNT/graphene composite exhibited a specific power density of 58.5 kW/kg and energy density of 62.8 Wh/kg which is ten times greater than that of activated carbon based supercapacitors, energy density further increased to 155.6 Wh/kg when ionic liquid is used as electrolyte.

Another problem causing the reduction of effective SSA of graphene is that electrolyte cannot fully wet the active materials. The electric double-layer cannot form at an

unwetted surface of graphene sheets and the reduced contact area of electrode/electrolyte leads to increased resistance and thus poor electrochemical performance. With high ionic conductivity, wide operation voltage windows (> 3V), outstanding thermal and chemical stability, room temperature ionic liquid has become promising next-generation electrolytes to boost the energy density of supercapacitors.[45] However, ionic liquids meet more serious wetting problems due to their high viscosity compared to traditional aqueous and organic electrolytes.

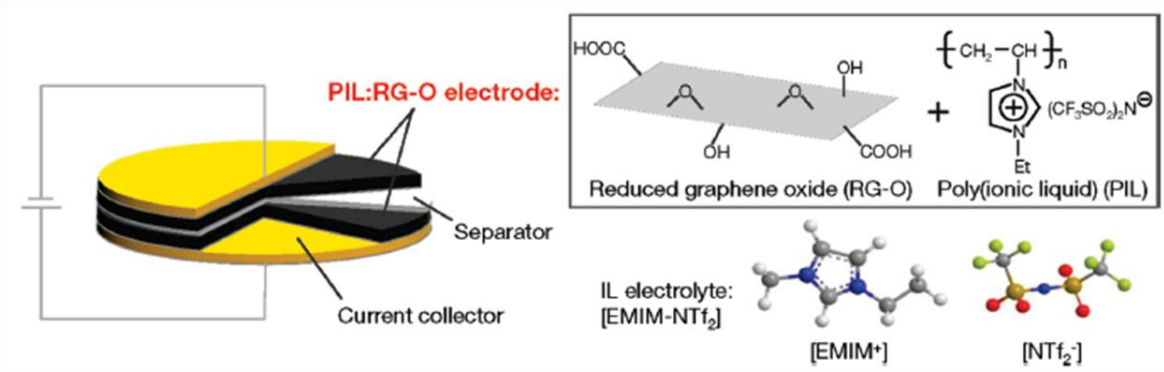

Figure 2.6: Three-dimension view of ideal graphene crystalline structure. (Reproduced from ref. 46)

Rao et al.[47] first utilized ionic liquids as the electrolyte in graphene-based supercapacitors. They prepared graphene electrodes by thermal exfoliation and after imbibing the ionic liquid, the supercapacitors exhibited a modest capacitance of 75 F/g and energy density of 31.9 Wh/kg at 60 °C. To further improve the compatibility between graphene-based materials and ionic liquid, Suh et al.[46] synthesized a poly(ionic-liquid)/rGO composite with 1-ethyl-3-methyllimidazaolium bis(trifluoromethanesulfonyl) imide ($EMImNTf_2$) as electrolyte (**Figure 2.6**). This advanced ultracapacior displayed an improved specific capacitance of 187 F/g which is much higher than those using pure graphene-based materials in ionic liquid.

Jang et al.[48] reported their work using crumpled graphene sheets with 1-ethyl-3-methylimidazolium tetrafluoroborate ($EMImBF_4$) as the electrolyte, and the resulting energy density at room temperature can achieve 85.6 Wh/kg at 1 A/g (further improved to 136 Wh/kg at 80 °C), which is comparable with Ni-MH batteries used in HEVs.

2.4 Goals and Layout of Thesis Work

The main goal of this thesis work is to develop new methods and a deeper understanding of how to increase the energy density of EDLCs while maintaining the other outstanding characteristics such as high power density and nearly unlimited cycle-life compared to current secondary battery technologies. To achieve this, we focus on the route to use graphene based materials in ionic liquids with a very large operating voltage window. As mentioned in Section 2.1.1, the energy density of a supercapacitor is directly proportional to the volumetric capacitance of a single electrode and the square of the operating voltage, so even a small extension to the working voltage or a significant enhancement to the capacitance at in a high voltage cell can lead to substantial improvements to device energy density. However, the main challenge for ionic liquid electrolytes has been described in the last section. The high viscosity and poor compatibility with active materials may significantly reduce the effective SSA for energy storage. To solve this problem, in Chapter 3, we first study an evaporative consolidation approach to prepare IL/H_2O/GO gels and improve their conductivity through thermal reduction at low temperature (360 °C). In this work, we try to introduce IL between GO at an early stage during the fabrication process so as to avoid the challenge to wet a dry graphene film. A hydrophobic (water immiscible) and hydrophilic ionic liquid (water miscible) are compared as electrolytes for this method. Moreover, the effect of the

thermal reduction temperature is studied considering the temperature limitations of different components in the electrode precursor.

In Chapter 4, we develop a new approach to combine ionic liquids with graphene using ionic liquid microemulsions. We first demonstrate a stable microemulsion of EMImTFSI/Tween 20/H_2O that exhibits a narrow diameter distribution (~8nm) of microemulsion droplets and prove that the microemulsion can spontaneously adsorb to the surface of GO by the formation of hydrogen bonding between Tween 20 and surface oxygen-containing functional groups of GO. Then the IL-containing microemulsion are used as "soft spacer" to maintain an appropriate space between graphene oxide sheets and release electrolyte (IL) into rGO sheets through a simple heat treatment to remove Tween 20 and reduce GO at same time. This method results in a dense and uniform IL-mediated rGO (IM-rGO), which exhibits very good electrochemical performance. In the final chapter, we put forward the present further analysis and future plans to solve a remaining challenge, the limited cycle life (thousands cycles) of our electrodes. We suspect that the suboptimal cycle-life is related to impurities introduced during the thermal reduction of GO and the evaporation/decomposition of the Tween 20, the complex multicomponent system poses a characterization challenge.

3 Enhancement of Double Layer Capacitance through Evaporative consolidation of Graphene Oxide / Ionic Liquid

In the following chapter, I explored the possibility to extend the new electrode fabrication method, which is designed by Dr. Pope in 2013,[49] to a more practical level. He used colloidal gels of graphene oxide in a water-ethanol-ionic liquid solution to assemble graphene-ionic liquid laminated structures for use as electrodes in electrochemical double layer capacitors. The main idea is that introducing a room temperature ionic liquid (RTIL) into reduced graphene oxide (rGO) sheets before drying and heat treatment, so this IL serves not only as electrolyte but also as the spacer to prevent graphene sheets from restacking and improve the electrolyte-accessible surface area (effective SSA). Differing from the previous work, here we drop cast the resulting GO/IL gel-like film onto more common metal substrates (e.g. Al, Cu) rather than expensive Pt disk. Two imidazolium based ILs, hydrophilic 1-ethyl-3-methylimidazolium tetrafluoroborate ($EMImBF_4$) and hydrophobic 1-ethyl-3-methylimidazolum bis(trifluoromethylsulfonyl)imide (EMImTFSI), are investigated to determine their applicability for the evaporative consolidation with GO. The relevant experiment results indicate that EMImTFSI displays better compatibility with this method. Furthermore, the thermal reduction method for GO/EMImTFSI nanocomposite film was optimized with regard to the temperature range, ramp up rate and cooling rate to achieve the best results.

Finally, ramping up from room temperature to 360 °C at 5 °C/min combined with rapid cooling was found to be the optimal condition to minimize the evaporation of the ionic liquid and maximize the conductivity of the resulting GO. The resulting capacitance as a function of EMImTFSI content also exhibits a similar performance on an Al substrate compared to that of $EMImBF_6$/rGO on Pt disk making the process more practical. Also, the corrosion problem of hydrophilic $EMImBF_4$ is effectively avoided by using hydrophobic EMImTFSI as electrolyte. This work was carried out as a preliminary optimization and to generate a control group for the study presented in Chapter 4.

3.1 Introduction

Supercapacitors or electric double-layer capacitors (EDLCs) are electrochemical energy storage devices which deliver energy in a very short time (up to a few seconds).[5-6] As we discussed above, the main difference between batteries and EDLCs is that EDLCs store energy only through the rearrangement of charges/ions resulting in the formation of electric double-layer (EDL) at the electrolyte/electrode interface. The fully physical energy storage mechanism makes supercapacitors exhibit a number of advantages (e.g. long cycle life and fast charge/discharge) but suffer from a relatively limited energy density. The specific energy is proportional to the square of operating voltage window multiplied by the specific capacitance, hence, improving both the specific capacitance and cell working voltage window is crucial for designing advanced EDLCs with high energy density.

The maximum operating voltage window of such a device is usually limited by the working stability of each component (e.g. electrolytes, active materials and current

collectors) involved in the whole charge/discharge process, usually these devices cannot be charged beyond a voltage which can cause the degradation of these components. Due to the square relationship between voltage window and energy density ($E \propto U^2$), the voltage limitation decided by material/electrolyte combination is the key factor for resulting energy density as shown in **Figure 3.1**. Since electrolytes bear localized charge, they have lower electrochemical stability compared to other components.[50] Hence, the

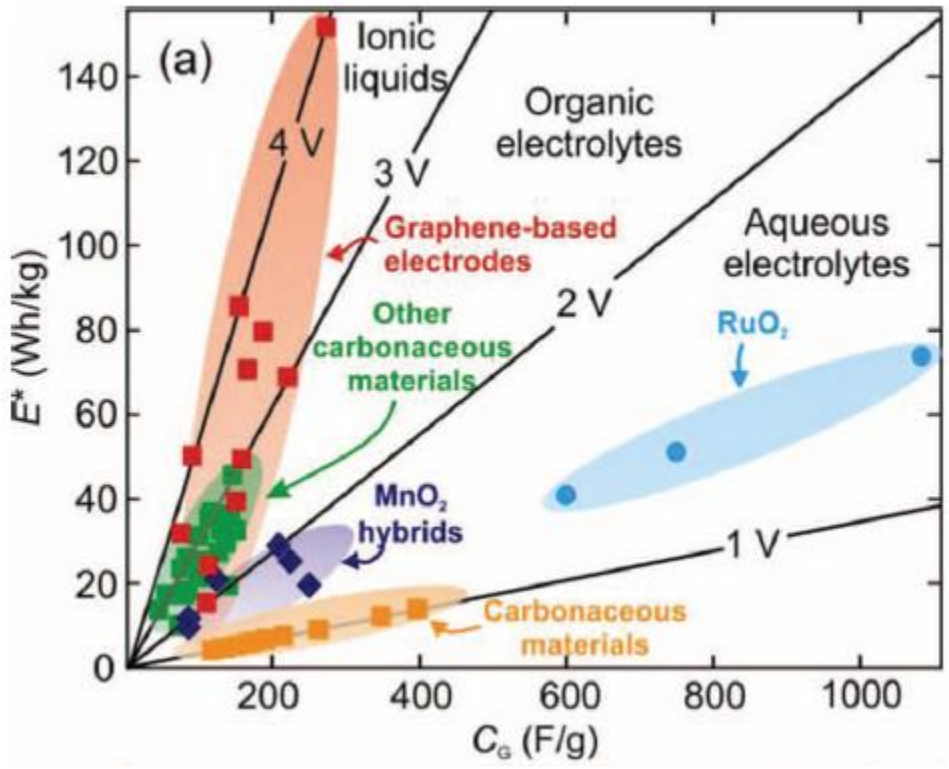

Figure 3.1: Estimated energy density as a function voltage window and gravimetric capacitance. (Reproduced from ref. 49)

choice of proper electrolyte is very important to extending the operating voltage window. Presently, aqueous, organic and ionic liquid based electrolytes are the three main types of electrolyte used in EDLCs.[14] Among these, the stable potential window of aqueous electrolytes is usually limited to below 1 V, and that of organic electrolytes (typically

based on acetonitrile or cyclic carbonates such as propylene carbonate) can be boosted to 3.5 V (limited by the decomposition potential of the solvent). However, IL-based electrolyte has been reported that can work stably at the voltage exceeding 5 V, which exhibit the largest operating voltage window among all electrolytes. Moreover, ILs typically have a very high decomposition temperature (> 300-400 °C), providing unique processing capabilities and allowing devices to work under extreme conditions (such as HEVs, which usually require the working temperature to be high as 60 °C and space applications which exhibit even more extreme temperature swings).[51]

Despite these advantages, there still are many challenges for IL-based electrolytes that need to be overcome. For graphene-based EDLCs, the main challenge is to more effectively combine high SSA graphene-based materials with IL-based electrolytes. The specific capacitance, another important parameter in determining the resulting specific energy density, is the product of intrinsic capacitance and SSA. Since EDLCs store energy mainly through the formation of a electric double-layer, so this SSA should be considered as the electrolyte-accessible SSA because the electric double-layer can only be generated at the electrolyte/electrode interface.[2] As highly viscous electrolytes, ILs are difficult to fully wet graphene-based materials (or other nanoporous electrode materials) and exhibit lower ionic conductivity compared to other electrolytes. Furthermore, spontaneous restacking of graphene sheets after exfoliation can decrease the SSA as well. To overcome these limitations, ILs are usually diluted by other organic solvent (e.g. acetonitrile, AN), as the bulk ionic conductivity of ILs based mixture is better than that of pure ILs due to the reduced viscosity. Bozym et al. diluted EMImTFSI by AN,[52] the bulk conductivity of mixture displayed a peak value of 36.1 mS/cm at 10.8 mol% the neat

EMImTFSI exhibits a conductivity of < 10 mS/cm. With the improved ionic conductivity, the differential minimum capacitance is also boosted from < 10 μF/cm^2 to 20.1 μF/cm^2.

Increasing the working temperature is also considered as one effective approach to ameliorate the relatively poor conductivity of ILs; in practice, energy storage systems are often required to operate at elevated temperatures in some specific applications.[7, 51] For example, supercapacitors are usually coupled with batteries or fuel cells in HEVs, to deliver the high power needed during acceleration as well as to collect energy from braking. Hence, operating temperatures of 60 ºC or more are currently required especially when these devices used are associated with fuel cells. With high decomposition temperature and outstanding electrochemical stability, IL-based electrolyte is the best choice to achieve the safe operation at elevated temperatures. Dagousset et al.[53] showed that the increase of temperature decreases the viscosity of ILs. The viscosity of EMImTFSI dropped from ~50 mPa·s at 25 ºC to ~20 mPa·s at 60 ºC, and relationship between viscosity and ionic conductivity also meets the Vogel-Tammann-Fulcher (VTF) behavior as commonly observed for ILs.

In addition to decreasing the viscosity by dilution or heating, many other strategies have been explored to modify the compatibility of ILs and graphene-based materials. So far, various solid components, including metal nanoparticles, metal oxide, polymers, carbon blacks and carbon nanotubes have been used as spacers between reduced graphene sheets to maintain its high SSA. Bozym *et al.*[54] used nanoparticles prepared via the dehydration of sucrose, a renewable feedstock, as spacers to prevent rGO sheets from restacking. They show that dehydrated sucrose effectively restrain the restacking of rGO and improve the specific capacitance from 115 F/g to $\leqslant$ 330 F/g. Kim et al.[46] synthesized

a poly(ionic liquid) (or called as PIL) as spacer by the polymerization of unsaturated salts. This PIL/rGO nanocomposite can be simply prepared by chemically reducing GO in propylene carbonate in the presence of PIL at 150 ºC. The surface modification of rGO sheets with hydrophobic PIL leads to a huge drop in contact angle between IL and rGO from 72º to 10º, indicating the improved ability of IL to fully wet rGO sheets. Recently, efforts are underway about how to use electrolyte itself as a "soft spacer" to avoid the introduction of other materials into graphene sheets. In this case, the IL would act as both electrolyte and spacer. Dan Li`s group[55] developed a chemically converted graphene (CCG) hydrogel via vacuum filtration of the CCG suspension within a volatile (organic solvent) and nonvolatile (IL) liquid mixture. Taking advantage of the capillary force during the evaporation of volatile liquid, the resulting IL mediated CCG film exhibits dense layered structure (1.33 g/cm^3) leading to a high volumetric capacitance of 212 F/cm^3 in AN/EMImBF$_4$ hybrid electrolyte at 1A/g. Almost concurrently, our group[49] designed a new method as shown in **Figure 3.2**. Instead of imbibing IL into rGO sheets after the formation of porous structure after reduction as shown in **Figure 3.2a**, we introduce IL (hydrophilic EMImBF$_4$) at an early step to form a water/IL/GO gel-like film followed by annealing. When the content of IL exceeds 60 wt%, the specific capacitance reaches the saturation value of 136 $\pm$ 10 F/g. The nearly constant value above 60 wt% suggests that the limiting ability to increase the electrolyte-accessible SSA by this method has been reached, and the additional IL (> 60 wt%) only contributed to the expansion of film thickness and introduced deadweight and volume to the electrode. However, Dan Li`s work cannot be scalable due to its vacuum filtration process. Chemical reduction of GO introduce more hazardous chemicals leading to increased cost for after-treatment.

Our previous work required expensive Pt current collector to avoid corrosion problems. And the gelation of GO/$EMImBF_4$ aqueous dispersion limited its potential to achieve a high loading of active materials by drop-casting. In this work, we use hydrophobic EMImTFSI as substitution to solve corrosion problem and make this evaporative consolidation method compatible with common current collectors (e.g. Al, Cu). Dispersing GO in an organic solvent (such as DMF) rather than water can prevent it from gelation, resulting in more uniform dispersions with lower viscosity. The resulting EMImTFSI/rGO on Al discs displayed a similar capacitive behavior as $EMImBF_4$/rGO on Pt discs with modified thermal reduction procedure.

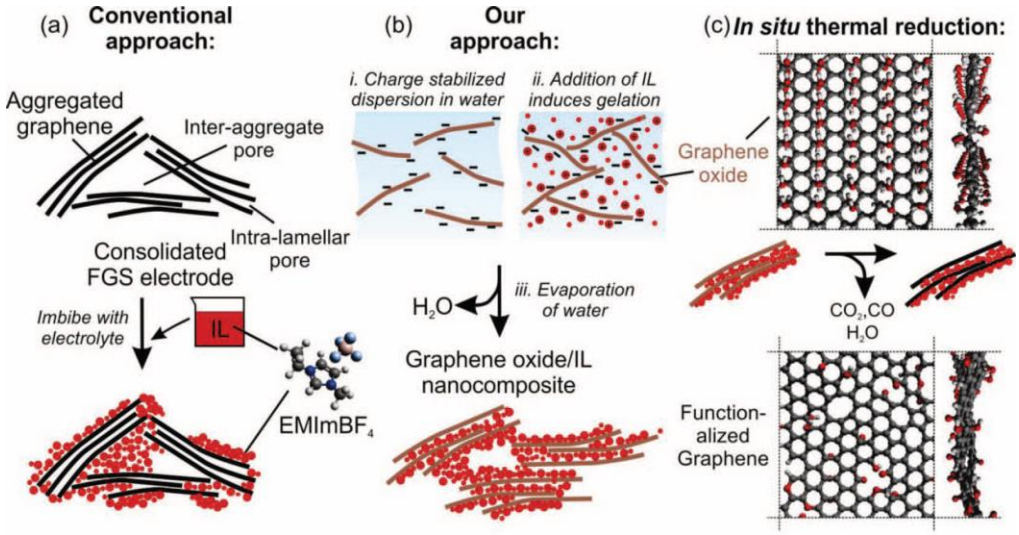

Figure 3.2: Schematic of conventional and out electrode fabrication approaches. (Reproduced from ref. 49)

3.2 Experimental

3.2.1 Synthesis of Graphene Oxide

GO was synthesized by a modified Hummer`s method, the brief preparation process is described as below. 3 g of graphite flake and 18 g of $KMnO_4$ were added into an acid

mixture composed of 360 ml of H_2SO_4 and 40 ml of H_3PO_4 under stirring. The following oxidation reaction was conducted at 50 ºC for 16 h. About 6 ml of H_2O_2 was added into the resulting mixture at it was cooled to room temperature along with the color change from purple to golden yellow. Then this suspension was distributed into six 50 ml centrifuge tubes and centrifuged for 30 min (3000 rpm, rotor diameter 15 cm). The supernatant was discarded, and the precipitating GO was dispersed by 30 % HCl and centrifuged again. The above washing step was repeated 3 times by 30 % HCl and 4 times by washing ethanol. The washed GO/ethanol slurry was stored for subsequent steps.

3.2.2 Electrode Fabrication

The above washed ethanol/GO slurry was diluted by washing ethanol to approximately 10 mg/ml. The electrode precursor suspension containing hydrophobic ionic liquid, EMImTFSI, was prepared by mixing the GO dispersion with N,N-dimethylmethanamide (DMF) at the volumetric ratio of 1:1. Then, 6 ml of this mixture was ultrasonicated at 50 % power for 30 min to make GO sheets disperse uniformly from its loose aggregation. EMImTFSI was added during the ultrasonication, a series of GO/EMImTFSI dispersions in DCE/H_2O mixtures were prepared with different amounts of EMImTFSI to achieve the IL content of 20-90 wt% in the final evaporated nanocomposite films. 150 µL of the resulting suspension was drop-casted onto 1 cm diameter Al discs (or copper foil) and allowed to slowly dry overnight at room temperature to eliminate the volatile components (i.e., water and DMF) while the non-volatile IL was retained in the film. The dried composite gel-like films were placed in a tube furnace in Ar atmosphere and thermally treated from room temperature (RT) to the

target temperature varied from 270 °C to 380 °C at a ramp rate of 5 or 10 °C/min. And then the reduced electrodes were cooled via a rapid way (exposed in air atmosphere at room temperature) or a slow way (cooled in the out-of-work furnace), the resulting sample is named as "X-Y-Z" where X, Y and Z are referred to as target temperature, ramp rate and cooling way, respectively. For example, 360-5-rapid represents that this film is reduced by heating from RT to 360 °C at 5 °C/min and then rapidly cooled down. The rGO/EMImBF$_4$ electrodes are produced by same recipe but DMF is substituted by deionized water (DI water).

3.2.3 Characterization of Electrodes

Electrochemical testing was carried out in a symmetric two-electrode configuration. Cells were assembled in an argon filled glove box (< 1ppm water and oxygen). Two rGO/IL nanocomposite electrodes and a porous polypropylene separator pre-soaked with EMImTFSI were sandwiched between stainless steel current collectors in a Swagelok cell without any binder, conductive agent or extra electrolyte. The gravimetric capacitance (C_G) of IL/GO electrodes were characterized by cyclic voltammetry (CV) at 5 mV/s, and calculated by:

$$C_{\mathrm{G}} = \frac{I_{\mathrm{ave}}}{v \cdot m}$$

Where I_{ave} is the average of reductive and oxidative current at mid-point of voltage window, v is scan rate and m is the single electrode mass of active material. The mass fraction of EMImTFSI in IL/GO composite is decided by thermogravimetric analysis (TGA Q500, TA instruments) which was performed in N_2 flow by heating the sample under nitrogen gas from RT to 600 °C at rate of 5 °C/min.

3.3 Results and Discussion

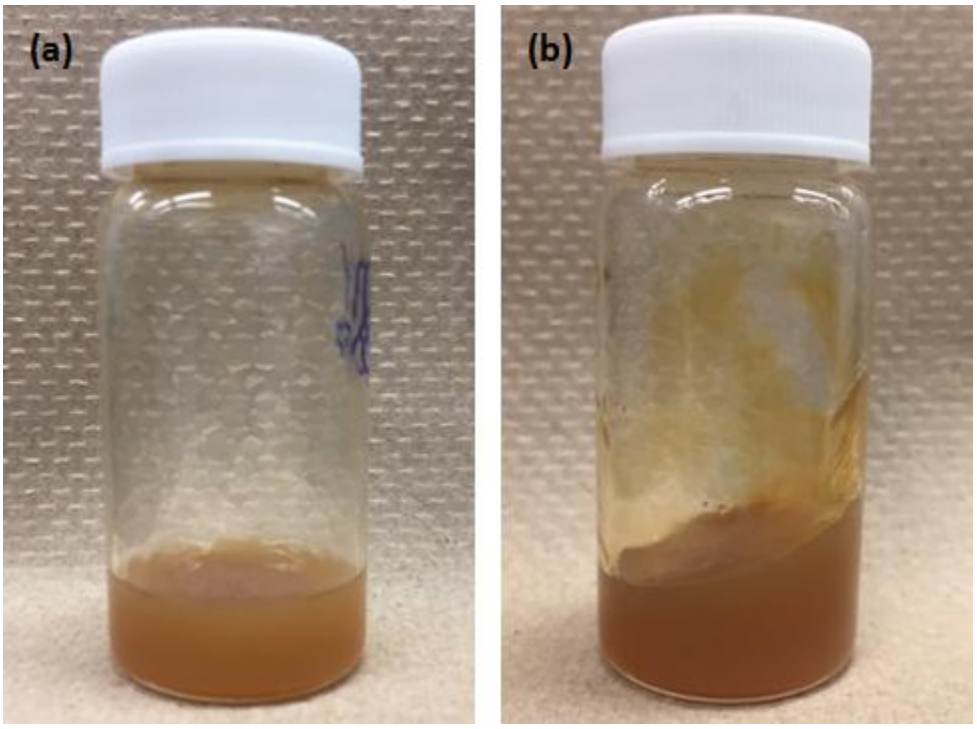

Figure 3.3: (a) GO/EMImTFSI dispersion in DMF/ethanol mixture and (b) GO/ $EMImBF_4$ dispersion in water/ethanol mixture after gently shaking.

Two ionic liquids, hydrophobic EMImTFSI and hydrophilic $EMImBF_4$, are investigated in this work to prepare IL modified rGO electrodes via evaporative consolidation. During the preparation of precursor IL/GO dispersion, 6 ml of GO dispersion (5 mg/ml) in ethanol/water mixture turns into a highly viscous slurry after the addition of $EMImBF_4$, while the GO/EMImTFSI mixture in ethanol/DMF is still at its original, flowing, liquid state. As shown in **Figure 3.3a** and **b**, GO/EMImTFSI dispersion can recover its original status immediately after gently shaking while the surface GO/$EMImBF_4$ dispersion remains at a certain angle. GO/$EMImBF_4$ dispersion restores its fluidity only after being diluted from 5 mg/ml to 2.5 mg/ml. The above observations suggest that the addition of $EMImBF_4$ causes a more significant increase in bulk viscosity

compared to EMImTFSI. Since GO is negatively charged in neutral or basic solution, this gelation phenomenon is ascribed to the screening of charge on the surface of GO sheets as a result of ionic strength increase, leading to partial aggregation of GO by interlayer van der Waals forcs.[56] Since Go sheets have better dispersibility in DMF than in water, this charge-induced flocculation is not problematic for the GO/EMImTFSI dispersion in the ethanol/DMF mixture. As the fluidity of precursor dispersion is an important factor which can help the viscous IL distribute uniformly between GO sheets to achieve the high electrolyte-accessible SSA in the following steps, EMImTFSI is the more practical choice here. In addition, dispersion with high fluidity is also more compatible with drop-casting than the thick slurry.

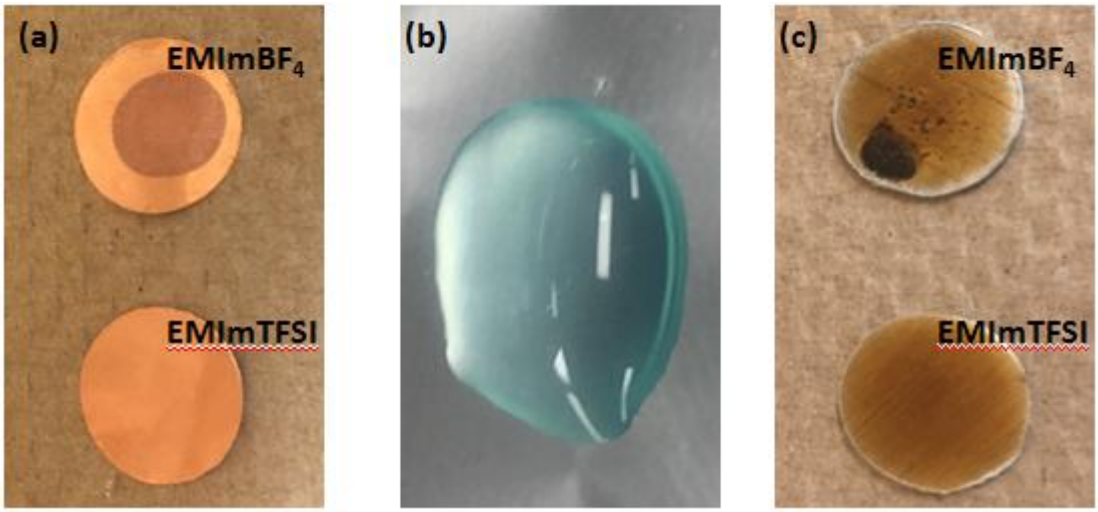

Figure 3.4: (a) $EMImBF_4$ and EMImTFSI drop on Cu foil; (b) $EMImBF_4$ drop after contacted with Cu foil overnight; (c) $EMImBF_4$ and EMImTFSI drop on Al discs.

The chemical stability on the common metallic current collectors was investigated for EMImTFSI and $EMImBF_4$. At room temperature, these two ILs were respectively dropped on Al discs and Cu foils and then observed the changes after overnight standing. For Cu foils, a corroded stain was caused by the pure $EMImBF_4$ drop as shown in the

Figure 3.4a while no apparent corrosion was obvious with the EMImTFSI case. The color of the $EMImBF_4$ drop changed from transparent to blue (**Figure 3.4b**) after overnight contact with the Cu substrate, suggesting the existence of Cu-containing ions. There was no corrosion observed for two IL drops on Al discs because Al has better chemical resistance compared to Cu. However, the Al disc was found to be corroded after being contacted with a drop of GO dispersion in water/DMF/$EMImBF_4$. A black corroded spot appeared on the Al disc as shown in **Figure 3.4c**. These negative effects are likely caused by the BF^- anion. Dilution of BF^- containing salts with water are known to induce hydrolysis of the BF^- to HF which can both solubilize the protective oxide layer on Cu and Al leading to corrosion.[57] Thus in addition to a lower viscosity of the GO dispersion, the EMImTFSI also displayed better chemical compatibility with common metal substrates compared to the water soluble $EMImBF_4$ salt. Hence, only EMImTFSI was used as electrolyte in the following experiments.

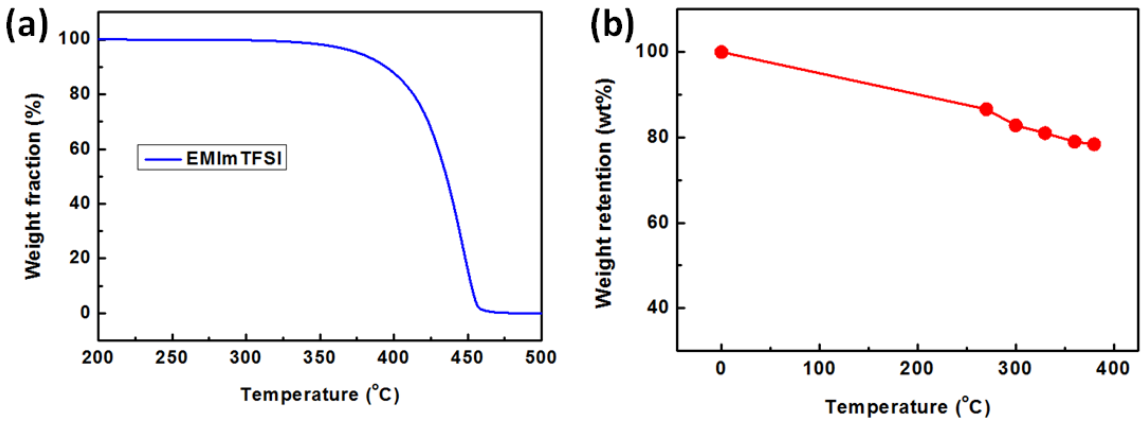

Figure 3.5: (a) TGA plot of EMImTFSI; (b) weight retention of GO with regard to its initial mass as a function of target temperatures (270, 300, 330, 360 and 380 °C).

To decide the available range of temperature settings to reduce the GO/IL precursor, TGA was carried out on pure EMImTFSI in Ar gas at the ramping rate of 5 °C/min as

shown in **Figure 3.5a**. According to the temperature dependent curve, EMImTFSI can be kept thermally stable up to as high as 350 °C. Above that, the decomposition or evaporation of EMImTFSI is gradually exacerbated with temperature, so the set temperature should be limited to be below ~350 °C to avoid too much loss of IL during thermal reduction. However, the initially insulating GO can be converted to conductive rGO with its increasing number of conjugated and aromatic carbon structures by heating (i.e., thermal reduction). Thermal reduction of GO typically begins at 200 °C but higher temperatures restore more of the graphene lattice and make the material more electrically conductive.[58] Hence, a series of values (270, 300, 330, 360 and 380 °C) were tested to determine an optimal temperature range which maximize the thermal reduction while minimizing the loss of IL. To calculate how much IL ought to be added to form the final rGO/IL electrode containing a specific content of EMImTFSI, the percentage mass retention of GO reduced by ramping up from room temperature to different target temperature at 10 ºC/min are measured and plotted in **Figure 3.5b**. With the increasing reduction temperature, more and more functional groups on the surface of GO sheets are decomposed to H_2O, CO and CO_2 gas resulting in the decreasing remaining solid mass.[59]

Table 3.1. Summary of IL retention and resulting gravimetric capacitance depending on varying target temperatures, ramp rates and cooling ways

Temperature (ºC)	Ramp Rate (ºC/min)	Cooling method	Content of EMImTFSI (%)	Capacitance (F/g)
270	5	Rapid	81.3	63
270	10	Rapid	81.7	60
270	10	Slow	80.7	62
300	5	Rapid	81	76

300	10	Rapid	81.2	74
300	10	Slow	74.5	78
330	5	Rapid	80.5	91
330	10	Rapid	80.9	83
330	10	Slow	62.4	54
360	5	Rapid	79.8	135
360	10	Rapid	80.1	121
380	5	Rapid	69.4	81
380	10	Rapid	72.7	86

To pursue the optimal thermal reduction settings, electrochemical characterization of the as-fabricated EMImTFSI/rGO composite electrodes were tested in a symmetric two-electrode system. According to different ramp rates (5 °C/min and 10 °C/min), target temperatures (270, 300, 330, 360 and 380 °C) and cooling ways (slow and rapid), the corresponding gravimetric capacitance (calculated from CVs at 5 mV/s) for each sample (target content of IL is ~80 wt%) is summarized in the **Table 3.1**. The target temperature significantly affected the final electrochemical performance as shown in **Figure 3.6a**, the area of the CV plots grew and became more like rectangular with rising temperature when other parameters are fixed. According to the table, the resulting gravimetric capacitance is boosted with temperature with sufficient IL (~ 80 wt%) until a significant decomposition occurred at > 360 °C (followed by rapid cooling) or > 300 ºC (followed by slow cooling). The reason for comparing the two cooling routes was based on the hypothesis that slow cooling could to maintain a more intact film due to the different thermal expansion coefficients between IL and rGO. However, experiment results

suggest that slow cooling aggravated the loss of IL leading to poor capacitance. Even for low target temperatures (≤ 300 ºC), slow cooling cannot improve capacitance too much although it helped us achieve more uniform films. The slower ramp rate was capable of

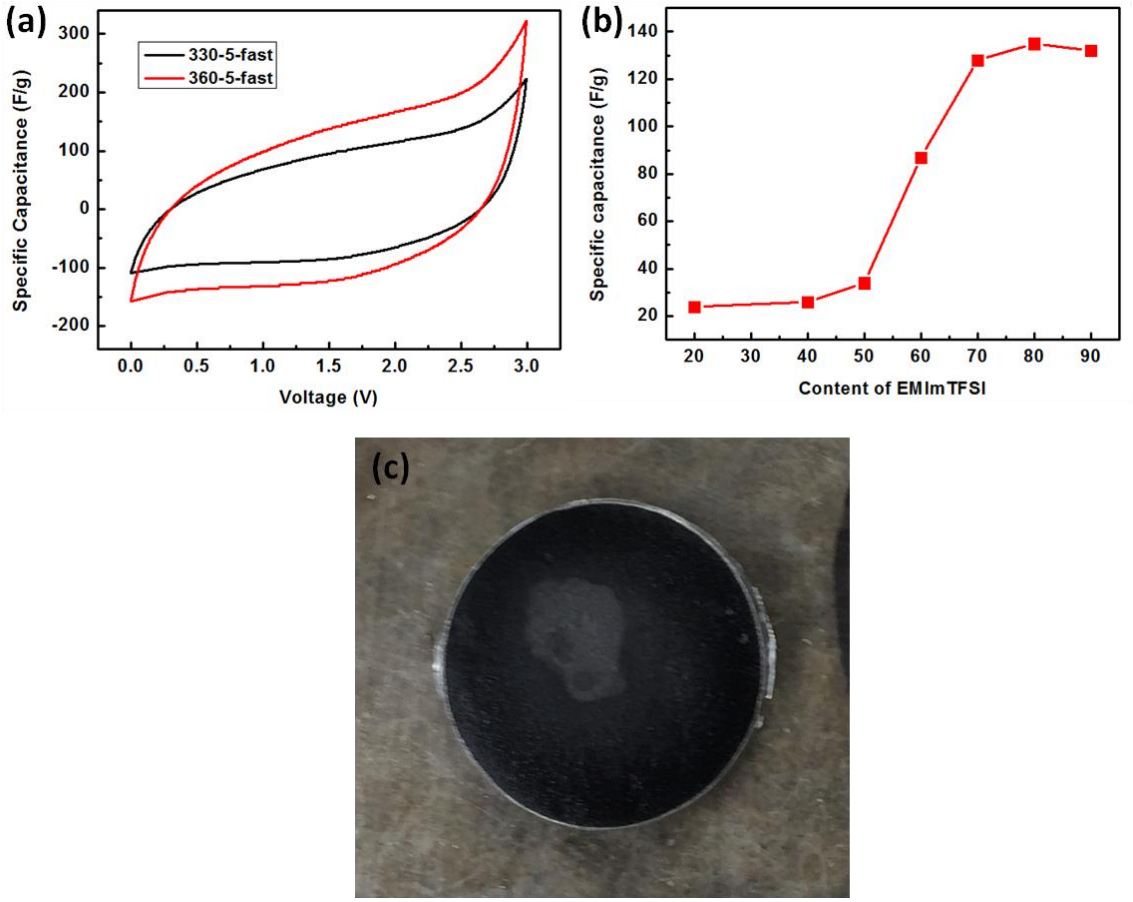

Figure 3.6: (a) CV plots of 330-5-rapid and 360-5-rapid at 5 mV/s; (b) gravimetric capacitance as a function or content of EMImTFSI; (c) digital image of reduced 360-5-rapid film.

better reducing the films by exposing them to heat for a longer duration of time. However, it should be mentioned that depending on the furnace size and shape, the optimum temperature may be slightly different due to differences in heat transfer rates. Through the above comparison and analysis, electrodes reduced by ramping up from room temperature to 360 °C at 5 °C/min followed by rapid cooling exhibit the best capacitance of 135 F/g. The capacitance exhibited by samples containing different percentages of IL

is plotted in **Figure 3.6b**, showing a similar changing tendency as our previous work. When the content of IL exceeds 50 wt% with regard to the bulk mass of IL/rGO film, the corresponding capacitance is increased from < 40 F/g to > 100 F/g. There is no significant improvement after 70 wt%, suggesting that the IL has fully wetted all rGO sheets and the additional IL does not expose any additional surface area. Furthermore, inspection of the films after reduction (see photograph in **Figure 3.6c)** shows an uneven distribution of IL between the rGO sheets with the optimal thermal reduction settings. This uneven distribution highlights the major shortcoming of this electrode fabrication method. Upon drying of the GO/IL dispersion, the distribution of IL around the GO sheets is not easily controllable. Thus while we were able to achieve a similar capacitance to our previous work, using a more stable IL and by casting onto Al or Cu foil current collectors (as opposed to Pt), we did not see any significant enhancement to capacitance and thus IL-accessible surface area achieved.

3.4 Conclusion

Due to the better chemical stability and compatibility, this work demonstrates that EMImTFSI is a more suitable IL for the evaporative consolidation and thermal reduction approach compared to $EMImBF_4$. By co-consolidation of GO and EMImTFSI, the EMImTFSI can be use as both a soft spacer and electrolyte in IL/GO composite electrodes. The optimum thermal reduction protocol for this IL/GO composite was found for our furnace by changing relevant heat treatment settings including ramping rate, target temperature and cooling method. Considering the trade-off between retention of enough IL and reduction degree of GO, the samples reduced from room temperature to

360 ºC at 5 ºC/min was found best to achieve a maximum capacitance of 135 F/g at 5 mV/s. However, the uneven distribution of IL within the films suggests that improved methods are required to enhance the capacitance and IL-accessible surface area to a greater extent. However, the ability to cast electrodes directly onto commercially relevant current collectors such as Cu and Al shows a great potential to boost relevant electrochemical performance by further modifying the method to make IL distribute more uniformly between graphene sheets.

4 EMImTFSI / Tween 20/ H_2O Microemulsions and their Spontaneous Adsorption onto GO Surfaces

In the following chapter I dispersed a hydrophobic ionic liquid, EMImTFSI, in deionized water through the formation of oil/water micrormulsion system with the existence of a non-ionic surfactant, Tween 20. To decide the minimum ratio of Tween 20 to EMImTFSI, mixtures with different composite was prepared and observed whether can form a stable and clear single-phase liquid. Ferricyanide is used as the chemical redox probe to determine the phase behavior of microemulsion containing varying content of water with constant amount of IL and Tween 20 at the ratio of 1 : 4. Three regions of microemulsions: water-in-EMImTFSI (water/oil), bicontinuous and EMImTFSI-in-water (oil/water) were identified according to redox peaks in corresponding cyclic voltammetry (CV) plots. EMImTFSI-in-water microemulsion is further investigated by dynamic light scattering (DLS), suggesting those nanodroplets present a very uniform distribution with average diameter of ~8 nm. To clarify the interaction between dispersed GO sheets in water and EMImTFSI microemulsion nanodropltes, a fluorochrome (rhodamine-b, Rh-b) was added as probe. According to corresponding fluorescence characterization, an

effective spontaneous adsorption of microemulsion nanodroplets onto GO surface is demonstrated and shows the potential to be used as spacer to distribute IL uniformly onto the surface of rGO sheets through evaporative consolidation. The results of this chapter have been submitted to ACS Nano. This manuscript is currently being revised based on reviewer comments.

4.1 Introduction

Microemulsions, also sometimes referred to as nanoemulsions, are optically transparent and thermodynamically stable colloidal dispersions. They can spontaneously form by mixing an oily phase, a water phase and a surfactant or emulsifier. In 1943, Hoar and Schulman[60] found that a cloudy sodium stearate / hexadecane / water emulsion changed to transparent after adding hexanol. For a long time, this transparent dispersion was known as hydrophilic oily micelles or lipophilic aqueous micelles. Until 1959, this stable and clear system was first named as "microemulsion".[61] Differing from a traditional emulsion, microemulsion are both kinetically and thermodynamically stable, and usually exhibit a dispersed phase with dimension typically in the range of 10 ~ 100 nm which is a size range that does not scatter visible light.

According to the ratio between the oil/water/surfactant, the microemulsion can be classified into three domains, water-in-oil phase (W/O), bicontinuous phase (B.C.) and oil-in-water phase (O/W). W/O microemulsions usually form when fraction of water with regard to bulk system is lower than a certain value. Tiny aqueous droplets (dispersed phase) surrounded by a surfactant (and possibly co-surfactant) molecules become thermodynamically stable in oil, which is the continuous phase. In contrary, water acts as

a continuous phase while oil becomes the dispersed phase resulting in an O/W microemulsion. When the amount of water and oil present are similar, a special structure called as bicontinuous microemulsion system may result. In this case, both water and oil exist as a continuous phase. Irregular channels of oil and water are intertwined, resulting in what looks like a "sponge-phase".[62-63] The phase behavior of microemulsion is usually characterized by constructing a ternary-phase diagram. For example, a $BMImPF_6$ / Tween 20 / water microemulsion was prepared by Gao er al.[64] and its ternary-phase diagram was constructed through continuous titration as shown in **Figure 4.1**.

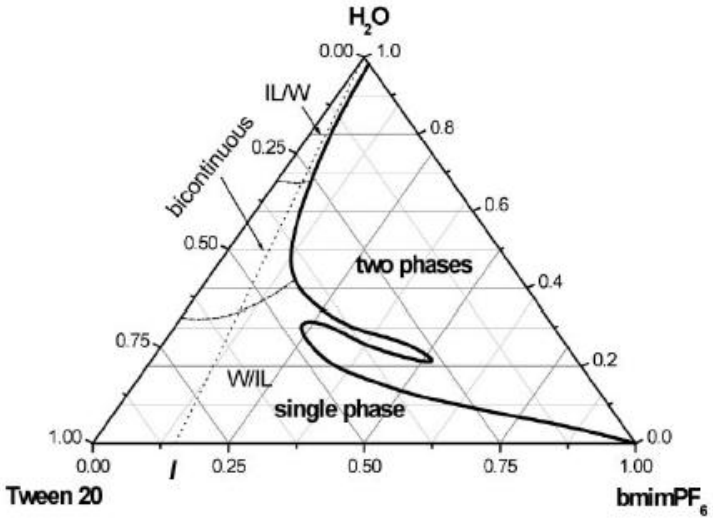

Figure 4.1: Ternary-phase diagram of bimimPF_6 / Tween 20 / H_2O. (Reproduced from ref. 64)

Many models have been constructed to explain the formation principle, such as mixed film theory,[61] solubilization theory[65] and thermodynamic theory.[66] Here, I briefly explain the formation from mixed film theory represented by Schulman, who was one of the first to work on microemulsion systems. Schulman et al. suggest that a microemulsion should be considered as a multiphase system whose formation is contributed by the process of interface growth. In this theory, surfactant (and probably co-surfactant) can form the third

phase, a layer of film, on oil/water interface. The existence of this surfactant film can significantly decrease the interfacial tension to a very low level, even lower than zero in some cases. Surface with negative interfacial tension is unstable, which prompt system extend its interface area spontaneously resulting in thermaldynamic stable dispersion with tiny size of dispersed droplets.

The common emulsifiers used for microemulsion preparation can be classified into two types, ionic surfactant (e.g. CTAB, SDS) and nonionic surfactant (e.g. Tween 20, Tween 80, Span 20, Span 80). A co-surfactant (e.g. ethanol, hexanol) is needed when using ionic surfactants to prepare the microemulsion. Co-surfactant molecules can speparate charged head groups on ionic surfactant molecular chains and subsequently weaken electrostatic repulsion between like charges. This makes the surfactant form a denser film at the oil/water interface leading to lower interfacial tension and shorter radius of curvature for the dispersed droplets. In this work, we characterized EMImTFSI/Tween 20/H_2O microemulsion from phase behaviors to size distribution, and demonstrated our hypothesis as shown in **Figure 4.2** by fluorescence quenching experiment.

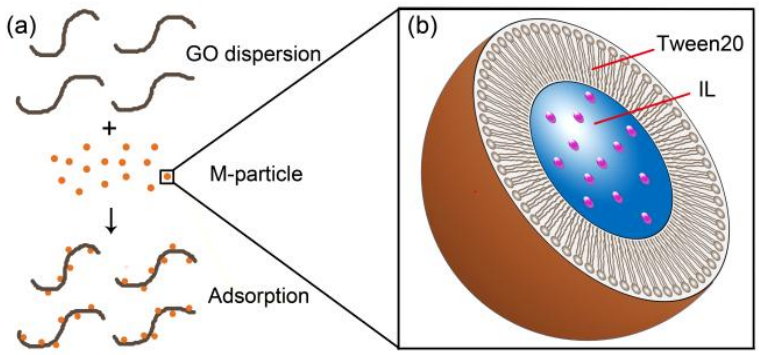

Figure 4.2 Schematic of the fabrication of ionic liquid mediated reduced graphene oxide. (a) Spontaneous adsorption of microemulsion particles on GO surface, (b) enlarged view of EMImTFSI/Tween 20/H2O microemulsion particles

4.2 Experimental

4.2.1 Characterization of EMImTFSI / Tween 20 / H_2O Microemulsion

CV testing was carried out at different scan rates (20-200 mV/s) using a three-electrode cell to probe the microstructure of the microemulsion by monitoring the apparent diffusion of the electrochemical probe ferricyanide. Glassy carbon was used as the working electrode, a platinum wire counter electrode and a Ag/AgCl reference electrode were used to test microemulsions containing 4 mM potassium ferricyanide (K3Fe(CN)6, Acros Organics) in 1 M KCl (Fisher Scientific)). The microemulisons were prepared using a fixed weight ratio of EMImTFSI to Tween 20 of 1:4, and the composition was varied by changing the mass fraction of water from 5 wt% to 90 wt%. For a diffusion-controlled system (**Figure 4.4b**), the micro-structure of the microemulsion can be inferred by the apparent diffusion coefficient which is determined by the Randles-Sevcik equation:[67]

$$i_{\mathrm{p}} = \frac{0.447F^{3/2}An^{3/2}D^{1/2}Cv^{1/2}}{R^{1/2}T^{1/2}}$$

where *F* is the Faraday constant, *n* is the number of electrons involved in reaction, *A* is the area of working electrode, *D* is the diffusion coefficient, *C* is the concentration of reactant, *v* is the scan rate, *R* is the gas constant and *T* is the absolute temperature. The effecitive size distribution of corresponding samples without $K_3Fe(CN)_6$ and KCl were determined by dynamic light scattering (DLS, Zetasizer Nano-ZS90, Malvern).

4.2.2 Spontaneous Adsorption of Microemulsion Nanodroplets on GO Surface Determined by Fluorescence Quenching

Fluorescence quenching experiments were carried out to verify the adsorption of IL/Tween 20 onto GO. In a typical experiment, 96 mg of EMImTFSI was mixed with 384 mg Tween 20 to form stable microemulsion in 6 ml deionized water and 6 ml of aqueous GO dispersion (5 mg/ml) by ultrasonication at 40% amplitude for fifteen minutes. Ionic liquid macroemulsion was prepared by dispersing 96 mg EMImTFSI in 6 ml deionized water by ultrasonication (same settings). 10 mM rhodamine-b (Rh-B, Sigma-Aldrich) was added as a fluorescence probe in each of the three systems. As-prepared samples were observed in a dark room under the excitation of a UV lamp (245 nm) before and after centrifugation (15000 rpm, rotor diameter 15 cm for 25 min). As a control experiment the test was repeated for IL macroemulsion without any fluorescence probe. The digital images were taken by a cell phone and the fluorescence intensity was measured using a Cary Eclipse fluorescence spectrophotometer (Varian).

4.3 Results and Discussion

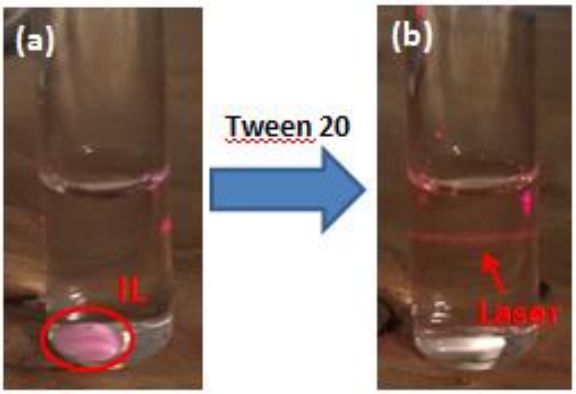

Figure 4.3. Characterization of neat IL microemulsion system. (a) Phase separated EMImTFSI in water (b) Transparent EMImTFSI/Tween 20/water microemulsion showing Tyndall effect.

As shown in **Figure 4.3**a, when EMImTFSI (labelled with a pink dye) is mixed with water, the two liquids phase separate. However, when Tween 20 is dissolved in water, the IL/water mixture becomes uniform and transparent under visible light (**Figure 4.3**b). When a laser beam is passed through the mixture it displayed a weak Tyndall effect suggesting the presence of a sub-micron-sized dispersed phase. These observations suggest the formation of a microemulsion similar to the system demonstrated by Yanan[64] et al. for ternary mixtures of $BMImPF_6$/Tween 20/water.

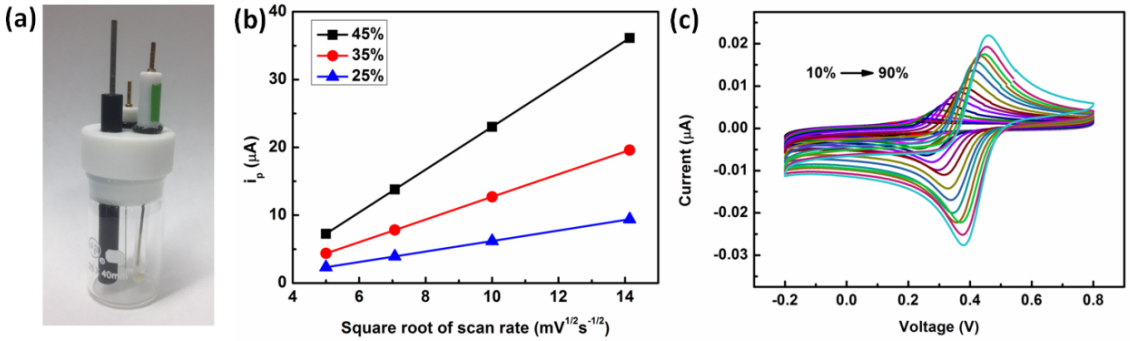

Figure 4.4. (a) Three-electrode testing system, (b) Scan rate dependence of peak current in EMImTFSI/Tween 20/H2O microemulsion containing 25 wt%, 35 wt% and 45 wt% of water, (c) CVs for microemulsions containing different amount of water varying from10 wt% to 90 wt% at 20 mV/s.

To identify the specific micro-structure of the microemulsion, the apparent diffusion coefficient (*D*) of the redox probe ferri/ferrocyanide was monitored, which selectively partitions into the aqueous phase.[67-68] The three-electrode system for CV tests used to determine the micro-structure of EMImTFSI/Tween 20/H_2O microemusion are shown in **Figure 4.4a**. Through changing the scan rate to observe the variation tendency of peak current i_p, it showed a linear relationship with $v^{1/2}$ at same testing condition but different slopes at three different contents of water (**Figure 4.4b**). This result indicates that the $[Fe(CN)_6]_3^{2-}/[Fe(CN)_6]_4^{2-}$ electrode reaction in the EmimTFSI/Tween 20/H_2O

microemulsion medium is diffusion-controlled which is an essential condition to apply the Randles-Sevick equation.[67] CVs of microemulsion with different content of water (10 wt% to 90 wt%) containing a highly reversible system (4 mM $K_4Fe(CN)_6$ in 1 M KCl) were carried at 20 mV/s. As shown in **Figure 4.4**c, the peak currents for microemulsions containing varying content of water were recorded to estimate the diffusion coefficient of chemical probe in the corresponding system. The shifting of the reaction half-wave potential is attributed to compositional changes in the system that could be described by the Nernst equation as discussed by Mackay et al.[68] As shown in **Figure 4.5a**, carrying out CV under diffusion limited condition, we obtain $D \propto i_p^2/C^2$ as a function of water content. Under water rich conditions, D is the largest in magnitude and nearly constant when the water content is higher than ~70 wt% indicating an IL-in-water microemulsion is formed in contrast to water lean conditions (< 30 wt%) where diffusion

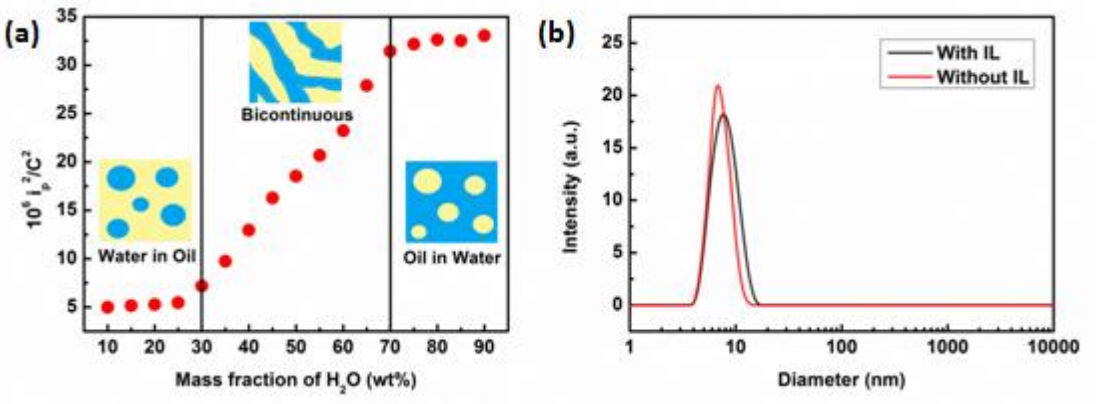

Figure 4.5. (a) The diffusion coefficient of K3Fe(CN)6 as a function of water content, (b) DLS showing the size distribution of Tween 20 micelles with IL and without IL.

is restricted. Between these two phases a bicontinuous phase likely exists but this was not investigated further. To use the IL in a formulation that could be cast onto electrodes, the water rich (> 70 wt%) condition was chosen for the rest of this work. As shown in **Figure 4.5b**, the effective size distributions of microemulsion particles and surfactant micelles at

90 wt% of water with and without IL were characterized by DLS. The hydrodynamic diameter of Tween 20 micelles (in the absence of added IL) was found to be ~ 6.8 nm, whereas that of the microemulsion was ~ 8.1 nm.

To study the interactions between dispersed GO sheets and the oil-in-water microemulsion particles (at water rich condition), we used a fluorescent marker Rh-B to identify specific adsorption of the IL microemulsion to GO through fluorescence quenching experiments.[69] As shown in **Figure 4.6a**, an extraction experiment illustrated that Rh-B (pink) strongly partitions into EMImTFSI. Exposure to UV light (~245 nm),

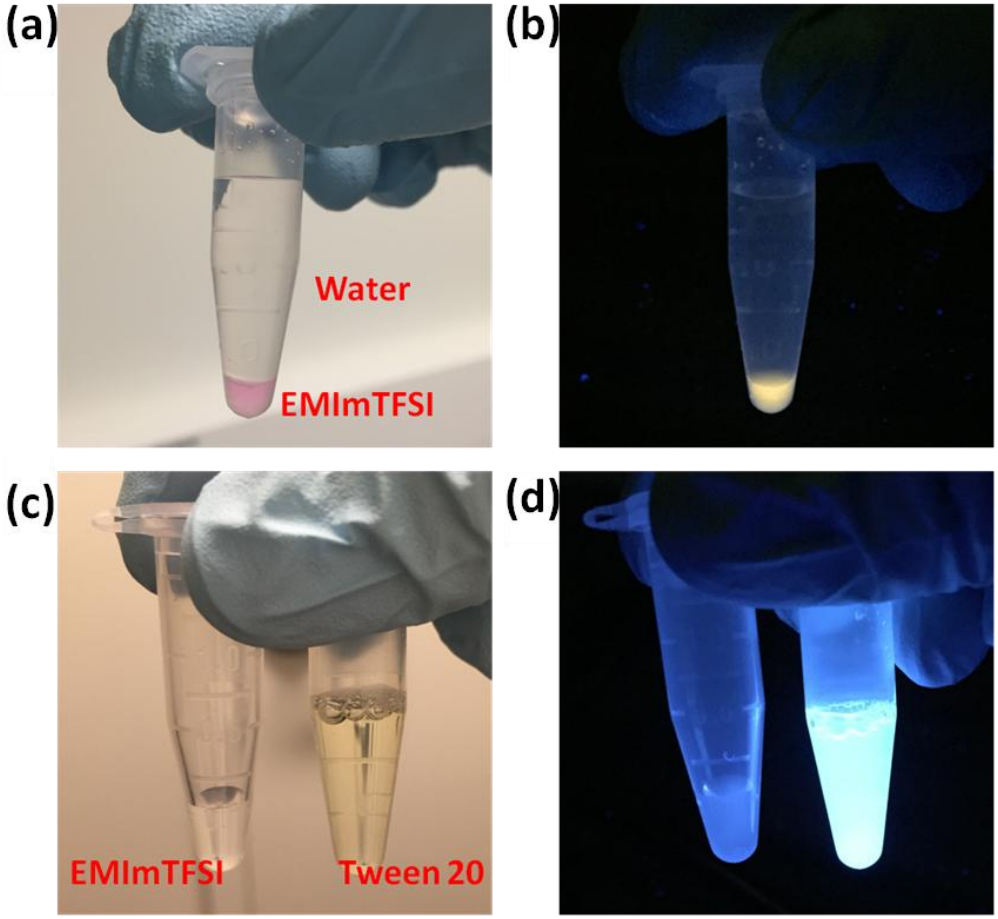

Figure 4.6. (a) Water/EMImTFSI mixture with Rh-b, (b) water/EMImTFSI mixture with Rh-b under the excitation UV light, (c) neat EMImTFSI and Tween 20, (D) neat EMImTFSI and Tween 20 under the excitation of UV light.

caused the Rh-B dissolved in the IL to fluoresce an orange color. As shown in **Figure 4.7(a, b)**, before and after centrifuging, the microemulsion (sample i) presented a whitish fluorescence response in contrast to the expected orange color exhibited by the dyed IL. Surprisingly, the Tween 20 surfactant was found to fluoresce a similar color in water (see **Figure 4.6**) suggesting that the fluorescence of Tween 20 masked that of Rh-B (orange fluorescent light). Despite this, Rh-B was still added to identify any potential separation between the surfactant and IL during the experiment. The IL itself did not fluoresce under the illumination used (sample iv). Adding GO to the microemulsion in a ratio of GO:IL:Tween 20 of 1:4:16 was found to suppress the fluorescence from both fluorophores (sample ii). After centrifuging the dispersion, the GO sheets sedimented and revealed a non-fluorescent supernatant (sample ii). For comparison, a macroemulsion was

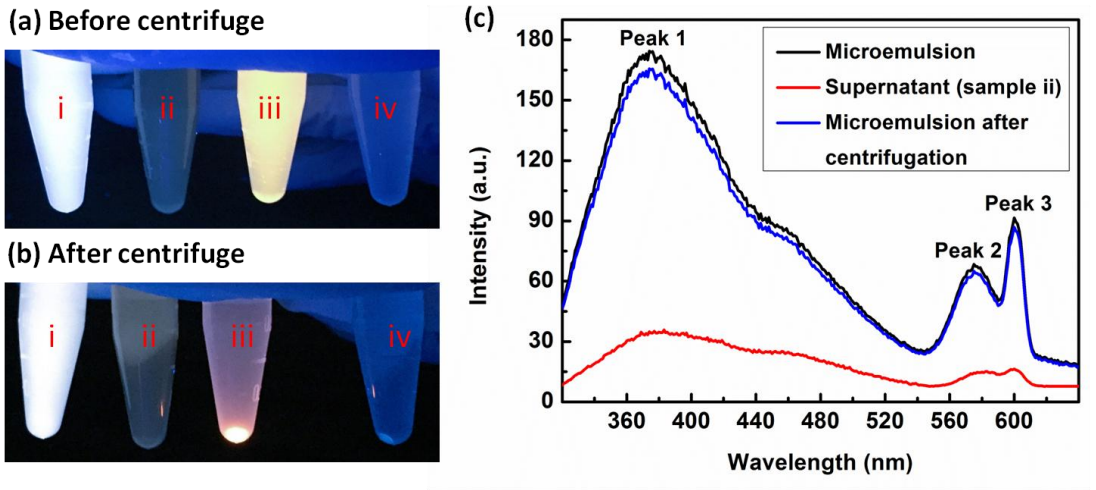

Figure 4.7. Fluorescence quenching experiments: Photos taken under the excitation of UV light before (a) and after (b) centrifugation for various mixtures: i. microemulsion of IL and surfactant in DI water + Rh-B, ii. microemulsion of IL and surfactant in aqueous dispersion of GO+ Rh-B, iii. EMImTFSI macroemulsion in DI water + Rh-B, iv. EMImTFSI macroemulsion in DI water without Rh-B; (c) plot showing the fluorescence intensity of the microemulsion before centrifuging and the supernatant remaining after centrifuging.

also prepared by ultrasonicating a mixture of IL in water without the surfactant both with and without Rh-B labelling (sample iii and iv, respectively). Immediately after

ultrasonicating, the emulsion was uniformly orange with the Rh-B present and was not fluorescent in its absence. In both cases, the IL quickly phase separated with the Rh-B remaining in the IL phase. These results suggest that the microemulsion particles, initially well-dispersed in the continuous water phase, spontaneous adsorb to GO. It is now well-known that GO effectively quenches fluorophores but only when the fluorophore is located several nanometers from GO surface – which is an important criteria for energy transfer.[69-70] From these results. we can conclude that the IL and surfactant must be within a few nanometer proximity of the GO surface. To quantify the change in fluorescence more accurately, the fluorescence intensity (**Figure 4.7c**) of the supernatant

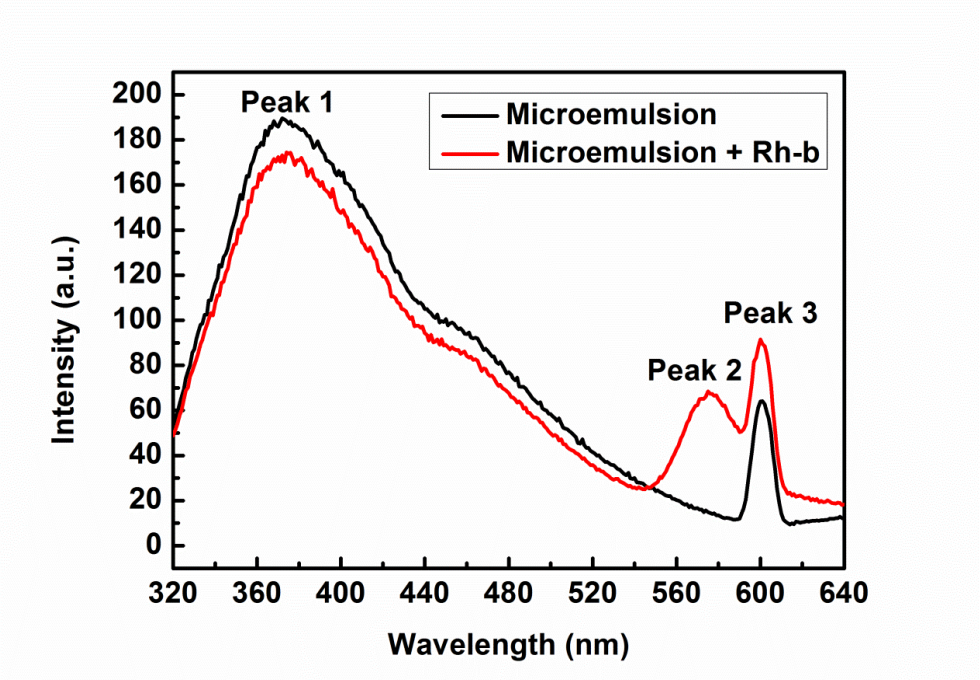

Figure 4.8. Plots showing the fluorescence intensity of the microemulsion with and without Rh-b.

taken from sample ii was tested and compared with that of the neat microemulsion both before and after centrifuging. There was no significant change in the fluorescence emission before and after the microemulsion was centrifuged. However, the fluorescence

intensity of the supernatant of the centrifuged GO/microemulsion mixture was significantly lower than the microemulsion alone but retained some residual fluorescence indicating that some microemulsion (or surfactant micelles) remained dispersed in the water phase at a low concentration. As shown in **Figure 4.8,** Peak 1 and Peak 3 are attributed to the fluorescence response of the microemulsion particles while the Peak 2 comes from Rh-b.[71]

Considering the reported structure of Tween 20 (**Figure 4.9a**), we attribute the driving force for adsorption of the microemulsion particles to the formation of hydrogen bonding between functional groups such as epoxides and hydroxides that are well-known to exist on the surface of GO, and the three terminal hydroxyl groups that exist on the polar head group of Tween 20.[72-73] The possible configurations are shown in **Figure 4.9b**, and classified into two types, (i) direct H-bonding and (ii) indirect H-bonding.

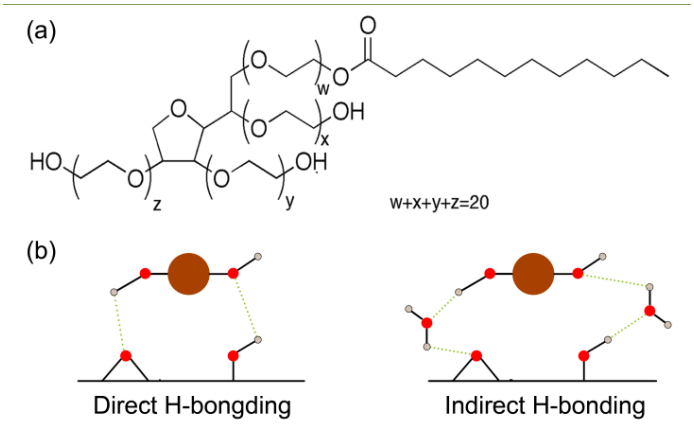

Figure 4.9. Possible interactions between GO and Tween-20: (a) Reported chemical structure of Tween 20; (b) schematic showing various configurations of hydrogen bonding between the microemulsion particles and GO sheets. The horizontal black lines denote the graphene oxide sheets while red, brown and grey dots represent oxygen, microemulsion particles and hydrogen respectively.

4.4 Conclusion

In this chapter, we successfully disperse hydrophobic ionic liquid, EMImTFSI, in water with the addition of nonionic surfactant, Tween 20. This system yields a thermodynamic stable and transparent dispersion, which exhibits a Tyndall effect when laser light passes through. At the fixed ratio of 1:4 between EMImTFSI and Tween 20, the phase structure of microemulsion changes from water-in-oil phase (content of water < 30 wt%) to bicontinuous phase (30 wt% < content of water < 70 wt%) and finally become oil-in-water phase at water rich condition (content of water > 70 wt%). And this microemulsion shows a homogeneous size distribution of ~8 nm according to DLS plots. To clarify the interaction between microemulsion nanodroplets and GO sheets, fluorescence experiments are conducted at water rich condition. The experiment results demonstrated that GO sheets can effectively adsorb microemulsion nanodroplets and significantly decrease the fluorescence intensity in the supernatant compared to microemulsion without the existence of GO sheets.

5 Decorating Grpahene Oxide with Ionic Liquid Nanodroplets: an Approach Leading to Energy Dense, High Voltage Supercapacitors

In the following chapter, a major stumbling block in the development of high energy density graphene-based supercapacitors has been maintaining high ion-accessible surface area combined with high electrode density. Herein we develop an ionic liquid (IL)-surfactant microemulsion system which is found to facilitate the spontaneous adsorption of IL-filled micelles onto graphene oxide (GO). This adsorption distributes the IL over all available surface area and provides an aqueous formulation that can be slurry cast onto current collectors, leaving behind a dense nanocomposite film of GO/IL/surfactant. By removing the surfactant and reducing the GO through a low temperature (360 °C) heat treatment, the IL plays a dual role of spacer and electrolyte. We study the effect of IL content and operating temperature on the performance, demonstrating a record high gravimetric capacitance (302 F/g at 1 A/g) for 80 wt% IL composites. At 60 wt% IL, combined high capacitance and bulk density (0.76 g/cm^3) yields one of the highest volumetric capacitances (218 F/cm^3, at 1 A/g) ever reported for a high voltage IL-based

supercapacitor While achieving promising rate performance and cycle-life, the approach also eliminates the long and costly electrolyte imbibition step of cell assembly since the electrolyte is cast directly with the electrode material. This chapter has been submitted for publication to ACS Nano and is currently being revised based on reviewer suggestions.

5.1 Introduction

Supercapacitors, also known as electric double-layer capacitors (EDLCs), are able to store energy rapidly and reversibly through the formation of a double-layer of electronic and ionic charge, closely spaced, at the electrode/electrolyte interface.[2, 74-75] Due to the combination of various advantageous properties, such as efficient operation at high power density, long cycle life and improved safety compared to Li-ion batteries,[7, 76] supercapacitors are being increasingly used as alternative power sources to rechargeable batteries. However, the implementation of supercapacitors in practical application is still restricted by the limited energy density, typically 5-8 Wh/L,[77] which is much lower than that of lead-acid batteries which can achieve ~50-90 Wh/L.[78] Considering a symmetric configuration, the volumetric energy density (E_V) of a supercapacitor is directly proportional to the volumetric capacitance (C_V) of a single electrode and the square of operating voltage (U) following the equation, $E_V = 1/8(C_V \cdot U^2)$. Therefore, in such a system, there are two ways to improve energy density: boosting capacitance and extending cell voltage window.

The operating voltage of EDLCs is typically limited by the stability of electrolyte and thus room temperature ionic liquids (ILs) with large electrochemical stability windows (> 3-4 V) have become promising next-generation electrolytes. However, the relatively

high viscosity of ILs results in lower ionic conductivity compared to traditional aqueous or organic electrolytes and also leads to challenges with pore wetting. Currently, there are two main strategies used to solve these problems: (i) diluting neat ILs with other organic solvents,[52] such as acetonitrile (AN), or (ii) increasing the working temperature of supercapacitors.[48, 53] On the electrode side, materials with a high intrinsic capacitance (C_{DL}) per area and a large ion-accessible surface area (SSA) are needed to achieve high gravimetric capacitance (C_G) since $C_G = C_{DL} \cdot SSA$. The potentially high electrical conductivity, surface area, and chemical stability of graphene-based materials make them promising candidate electrode.[36, 38] Theoretically, single layer graphene can exhibit SSA as high as 2675 m^2/g. While pristine graphene is limited by its low quantum capacitance leading to C_{DL} ~3-4 $\mu F/cm^2$, more defective and functionalized graphene produced by the chemical or thermal reduction of graphene oxide have been shown to exhibit $C_{DL} > 17\ \mu F/cm^2$ in non-aqueous electrolyte leading to theoretical gravimetric capacitance, $C_{G,theoretical} > 450$ F/g if all of graphene's surface area could be made ion-accessible. Another practical design constraint is the requirement to achieve this high surface area in the most dense configuration to maximize C_V since $C_V = \rho_{bulk} \cdot C_G$ where ρ_{bulk} is the bulk density of the graphene-based material. For example, achieving a high $\rho_{bulk} = 1\ g/cm^3$ could lead to $C_V > 450\ F/cm^3$ while the highest value reported in ILs-based electrolyte to date[55] ($212\ F/cm^3$) is much lower due to a combination of sub-optimal IL-accessible SSA and ρ_{bulk}.

To prevent aggregation and restacking of graphene-based materials into lower SSA structures, there have been numerous studies that use physical spacers to keep the sheets separated. For example, several reports use conductive spacers like carbon black,[79]

carbon nanotubes (CNTs)[80] or carbonized sucrose[54] to help maintain a high SSA. While promising, these approaches increase the dead weight and volume in the electrodes reducing the energy density of the device. More recently, there have been several approaches which avoid the use of non-graphene-based materials in the electrode formulation by using either a liquid[81-82] or the electrolyte itself[49, 55] as a spacer. For example, Yang et al.[81-82] demonstrated that solvation forces between chemically converted graphene (CCG) could be used to prevent restacking. This solvent could be exchanged with an IL electrolyte directly.[55] Improving upon this method, the same group recently demonstrated that a mixture of volatile solvent and non-volatile IL electrolyte could be introduced during vacuum filtration and the capillary forces acting during drying could increase ρ_{bulk} up to 1.25 g/cm^3 while the remaining IL acted as a liquid spacer. This high bulk density and the ability to achieve $C_G \sim 170$ F/g led to one of the highest reported C_V of 212 F/cm^3 at 1 A/g. However, the actual value is likely lower as the authors used ρ_{bulk} measured prior to soaking their electrodes in IL in their calculation, which may have caused the material to swell prior to cell assembly. Around the same time, we used a similar approach but instead drop cast graphene oxide (GO)/IL gels to create a dense nanocomposite for which the IL acted as a liquid spacer and the GO could be thermally reduced without loss of the temperature stable IL.[49] This approach led to a C_G = 140 F/g but at a lower bulk density of ρ_{bulk} = 0.46 g/cm^3 leading to C_V = 65 F/cm^3. While the casting approach and thermal reduction method used may be more scalable, it resulted in a lower ρ_{bulk} than vacuum filtration which is known to create well-aligned sheets and thus a higher packing density.[55, 83-85] Furthermore, while the film was co-consolidated with IL, there were no interactions between the IL used and GO sheets that

might facilitate wetting of the entire surface area causing the IL to be distributed randomly and leading to a sub-optimal capacitance. Building upon this approach, the focus of the current work is to design a system that facilitates the uniform distribution of IL around each graphene oxide sheet while maintaining a process compatible with conventional electrode slurry casting approaches.

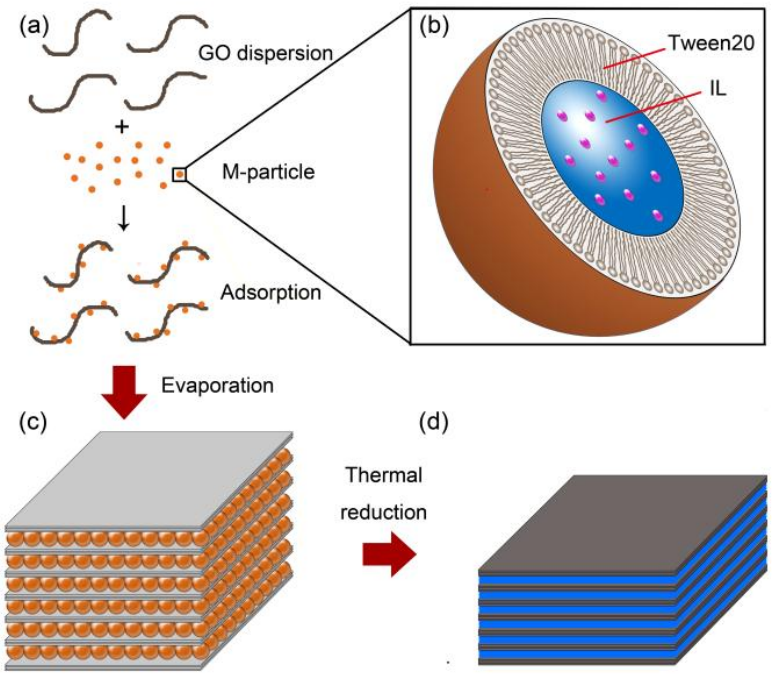

Figure 5.1. Schematic of the fabrication of ionic liquid mediated reduced graphene oxide. (a) Spontaneous adsorption of microemulsion particles on GO surface, (b) enlarged view of EMImTFSI/Tween 20/H2O microemulsion particles, (c) film structure after drop-casting and water evaporation, (d) film structure without Tween 20 after thermal reduction.

To achieve this goal, in this work, we demonstrate an IL microemulsion system (**Figure 5.1**) that spontaneously assembles on the surface of GO, placing nanometer-sized droplets of a high-performance, hydrophobic IL 1-ethyl-3-methylimidazolium bis(trifluoromethylsulfonyl)imide (EMImTFSI) directly onto the available surface of well-dispersed single layers. We first demonstrate that a common non-ionic surfactant,

Tween 20 is capable of forming a stable microemulsion with EMImTFSI with a particle size on the order of several nanometers. These surfactant stabilized nano-droplets (microemulsion particles) spontaneously adsorb to graphene oxide yielding a dispersion which can be cast directly onto current collectors leading to a dense nanocomposite of GO/IL/Tween 20. Tween 20 is then removed by evaporation, while the GO is thermally reduced leading to what we refer to as layered IL-mediated reduced graphene oxide (IM-rGO) electrodes. The approach is found to yield high ion-accessible SSA as evidenced by one of the highest C_G ever reported (302 F/g) when the composite contains 80 wt% IL. These results indicate that the microemulsion particles formed were better able to deploy IL as a spacer to prevent rGO sheets from restacking. Reducing the IL content to 60 wt%, resulted in dense electrodes that exhibited a $C_V = 218$ F/cm^3, which is the highest value reported to date among all graphene-based supercapacitors leading to exceptional volumetric energy density.

5.2 Experimental

5.2.1 Preparation of IM-rGO Electrodes

Graphene oxide (GO) was synthesized from natural flake graphite (Alfa Aesar) by Tour's improved Hummer's method.[49] The resulting GO had a ratio of C/O ~ 1.6 as determined by X-ray photoelectron spectroscopy (XPS) and no graphite peak which is characteristic of well-oxidized GO.[86] To 6 ml aqueous dispersion of GO (10 mg/ml), a predetermined amount of Tween 20 (Sigma-Aldrich) was added and ultrasonicated at 40% amplitude for fifteen minutes followed by the addition of EMImTFSI (Io-Li-Tec, 99% purity) and then was ultrasonicated at 40% amplitude for thirty minutes. A series of

GO/Tween 20/EMImTFSI dispersions were prepared with fixed mass ratio between Tween 20 and GO of 4:1 while the amount of EMImTFSI was varied to achieve a final IL content of 20-90% in the final composite. Typically, 150 μL of the resulting mixture was drop cast onto copper disks of 1 cm diameter and allowed to dry at room temperature (RT) for 12 hours, this recipe results in 1.5 mg/cm^2 of rGO, other areal mass loadings (0.75 mg/cm^2 and 4 mg/cm^2) can be achieved by changing the concentration of GO dispersion and volume of drop casting. And it should be noted that most tests in this paper were done at mass loading of 1.5 mg/cm^2 unless the special declaration. The partially dried composite gel-like films on Cu disks were then placed in a tube furnace in Ar atmosphere and thermally treated from RT to 300 °C at a ramp rate of 5 °C/min and preserved isothermally for 3 h to remove Tween 20 and then ramped to 360 °C with same rate. To prevent significant loss of EMImTFSI at high temperature, the disks were immediately removed from the furnace after it reached the set point. SEM images of IM-rGO electrodes were observed through a field emission scanning electron microscope (FE-SEM, LEO 1550, Zeiss) with an acceleration voltage of 10 kV. Thermogravimetric analysis (TGA Q500, TA instruments) was performed by heating the sample under nitrogen gas from RT to 600 °C at rate of 5 °C/min.

5.2.2 Fabrication of IM-rGO//IM-rGO Supercapacitor

Electrochemical testing was carried out in a symmetric two-electrode configuration. Cells were assembled in an argon filled glove box (< 1ppm water and oxygen). Two IM-rGO electrodes and a porous polypropylene separator pre-soaked with EMImTFSI were sandwiched between stainless steel current collectors in a Swagelok cell without any

binder, conductive agent or extra electrolyte. X-ray diffraction (XRD) measurement was obtained from XRG 3000 X-ray diffractometer (CuK_α radiation). The electrochemical properties of IM-rGO electrodes were characterized by cyclic voltammetry (CV), galvanostatic charge/discharge (GCD) tests and electro-chemical impedance spectroscope (EIS) on a computer-controlled potentiostat (SP-300, BioLogic). The C_G, areal capacitance (C_A) and volumetric capacitance (C_V) were calculated by following equations:

$$C_{\mathrm{G}} = 2\frac{i \cdot \Delta t}{\left(U - U_{\mathrm{drop}}\right) \cdot m}$$

$$C_{\mathrm{A}} = C_{\mathrm{G}} \cdot \rho_{\mathrm{A}}$$

$$C_{\mathrm{V}} = C_{\mathrm{G}} \cdot \rho_{\mathrm{bulk}}$$

where *i* is the corresponding current set in GCD tests, *Δt* is the time needed discharge the cell from 3 to 0 V, U = 3 V while U_{drop} is the voltage drop at the reversal of the scan direction due to the Ohmic losses, m is the mass of rGO on one electrode. ρ_{A} and ρ_{bulk} denote the areal density (i.e., mass per area) and bulk density (i.e., mass per volume) of rGO, respectively.

5.3 Results and Discussion

As shown in **Figure 5.2**a electrode films could be easily cast onto copper or aluminium current collectors from aqueous dispersions of the GO with the adsorbed microemulsion particles, yielding a dense, dark brown film. XRD profiles of the films (**Figure 5.2d**) taken immediately after drying indicated that the reflection associated with the interlayer spacing of GO (at 2θ ~ 9°) shifts to smaller scattering angle (2θ ~ 7.5°)

with 20 wt% IL (surfactant-free basis) and broadens. For higher loadings of IL, the films become X-ray amorphous. These observations suggest that the adsorbed microemulsion significant disrupts the restacking of the GO during evaporative drying and may act as a spacer to keep the sheets physically separated as schematically illustrated in **Figure 5.1c** and **1d**. In order to remove the insulating surfactant and not the IL, TGA was carried out on both neat EMImTFSI and Tween 20 to determine the optimal heat treatment temperature (**Figure 5.2**b). Tween 20 starts to degrade around 275 °C while EMImTFSI is stable to about 350 °C implying that there is a relatively wide range of temperatures that could be used to remove the Tween 20 but retain the IL. On the other hand, thermal analysis of IM-rGO electrodes containing 60% and 80% IL are shown in **Figure 5.2c**. In comparison to the pure IL, the mass loss corresponding to the decomposition of EMImTFSI in the IL/rGO composite shifted from around 350 °C to 300 °C. This may be

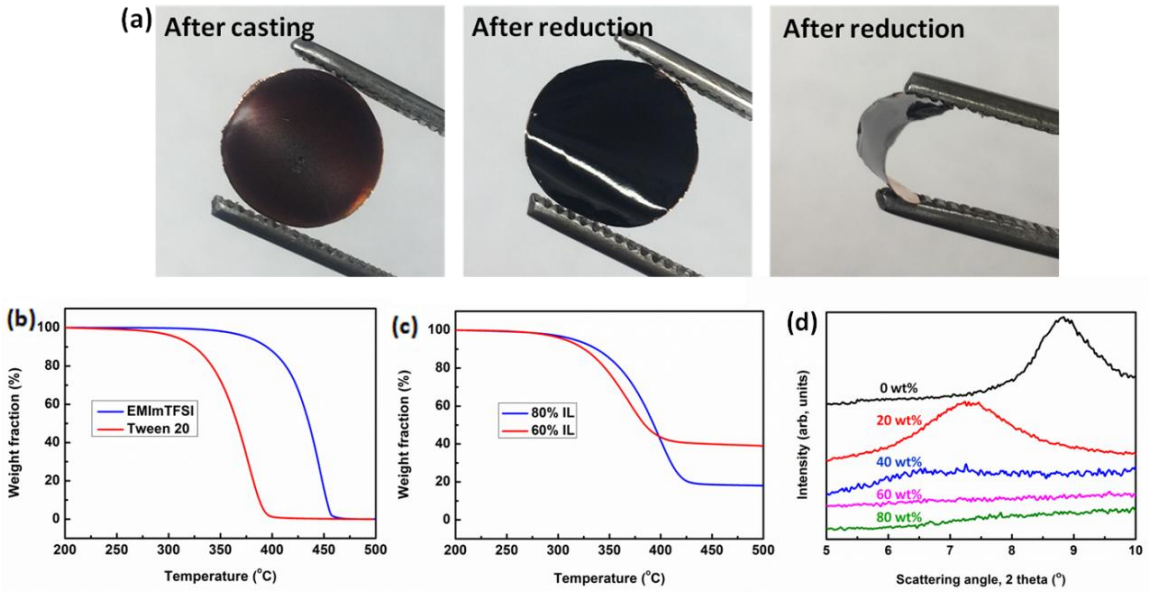

Figure 5.2. (a) Digital images of an air dried film on Cu disk after 12h (left), the electrode after removal of Tween 20 and thermal reduction of GO (middle), the reduced electrode showing flexibility (right); TGA plots of neat EMImTFSI and Tween 20 (b), and IM-rGO electrodes containing 60 wt% and 80 wt% of EMImTFSI (c); (d) XRD profiles for GO/microemulsion nanodroples films containing different content of EMImTFSI varing from 0% to 80%.

attributed to the high thermal conductivity of rGO[32] as well as their high absorbance[87] which accelerated the rate of diffusive and radiative heat transfer to the EMImTFSI. Thus heat treatment of the films near the limit of IL stability (300-360 °C) was carried out to remove the surfactant. As shown in **Figure 5.2a**, the heat treated films turned black and were mechanically robust enough to exhibit some flexibility even without binder. This mechanical integrity likely arises from capillary forces induced by an at least partially wetting IL film between rGO sheets.

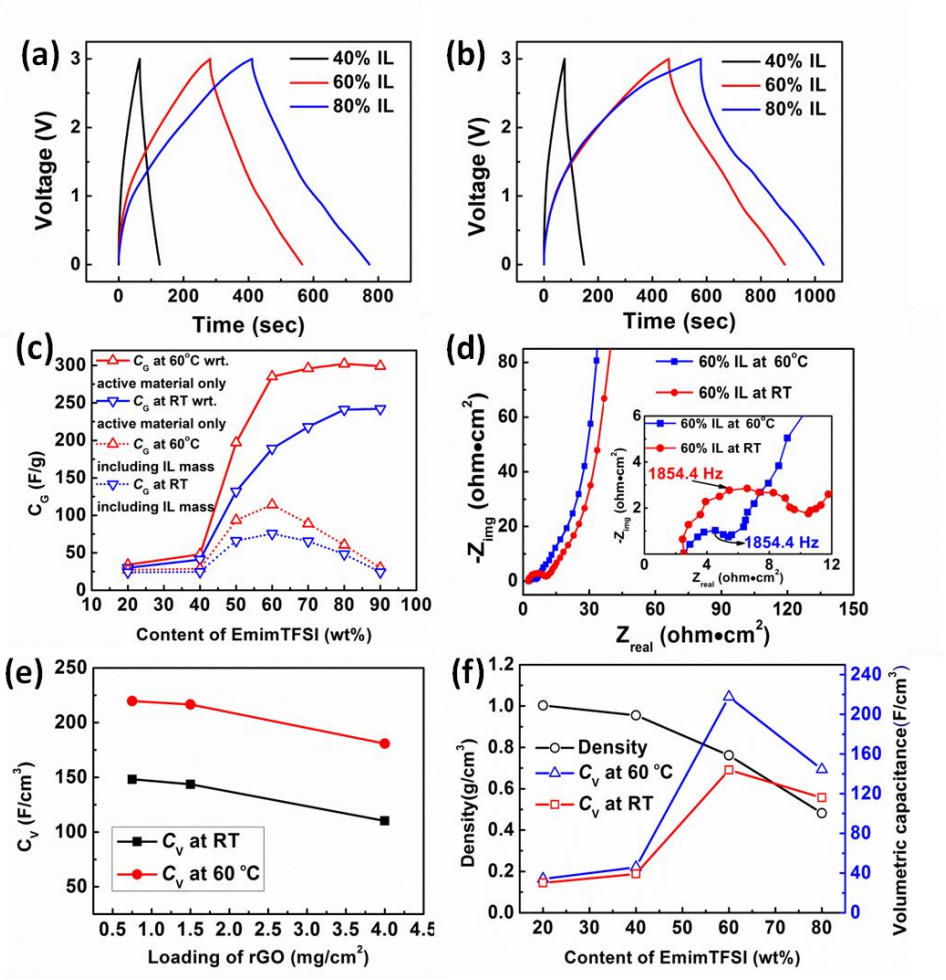

Figure 5.3. GCD plots of the IM-rGO electrodes with 40%, 60% and 80%-IL at room temperature (a), and at 60oC (b); (c) variation of gravimetric capacitance as a function of IL content in the IM-rGO electrode at 1 A/g, (d) Nyquist plot for IM-rGO electrodes with 60%-IL at different temperatures, (e) Volumetric capacitance as a function areal mass loading of rGO, (f) packing density and volumetric capacitance at different IL contents.

Electrochemical characterization of the as-fabricated IM-rGO electrodes was carried out in a symmetric two electrode assembly, without additional IL, by CV, GCD and EIS. As shown in **Figure 5.3a**, to determine the optimal amount of IL in the IM-rGO electrodes, a series of IM-rGO electrodes were prepared with varying IL content (i.e., measured after casting, drying and thermal treatment) from 20% to 90% and were tested at 1 A/g. With increasing IL content, from 40% to 60%, the electrodes showed a sharp increase in C_G from 41 F/g to 189 F/g and a relatively slow increase in gravimetric capacitance was observed on further increasing the IL content up to 80%. The IM-rGO electrodes with > 80% IL did not exhibit any significant increase in C_G indicating that 80% IL is the threshold value to wet the full ion-accessible SSA of the IM-rGO electrode at room temperature. The maximum C_G obtained from the IM-rGO electrode at RT was 241 F/g with 80% IL content.

In order to determine the impact of ionic conductivity on our results, we also cycled another set of electrodes, over the same IL content range, at 60 °C. Example GCD plots of the IM-rGO electrodes at 60 °C with different IL content are shown in **Figure 5.3b** and C_G as a function of IL content is summarized in **Figure 5.3c**. Similar to the RT observation, a significant increase in C_G is observed above 40% IL, reaching 285 F/g at 60% and up to 302 F/g at 80%. There was no further improvement at 90%. In fact, a slight decrease was consistently observed in both the RT and 60 °C cases. This could indicate loss of electrical contact between rGO sheets as is expected under low solids loadings. While testing at 60 °C has been carried out by others to ameliorate the low ionic conductivity of ILs, it is more common practice to reduce the electrolyte viscosity (thus increasing the conductivity) by diluting the IL with low viscosity solvents like

acetonitrile.[55, 88] While this solvent dilution approach could also be used here, recent studies have shown that dilution can increase not only the conductivity but also the intrinsic double-layer capacitance.[52] Addition of solvent after rGO/IL composite formation could also affect the spatial distribution of IL within the composite. To avoid these potential effects we instead changed the temperature; in practice, energy storage systems are often capable of operating at these elevated temperatures.[45, 51]

The C_G of the IM-rGO electrode increased more rapidly at 60 °C than the RT case at lower IL content but more slowly between 60% and 80%. It is well-known that the surface tension of liquids decreases with increasing temperature. In particular, it was recently shown that imbibing IL at higher temperatures improves wetting and the IL-accessible surface area of carbonaceous materials.[89] The improvement in ionic conductivity is also evidenced by the EIS results shown in **Figure 5.3d**. For both temperatures, a high frequency semi-circle is apparent in the Nyquist plots that is typically attributed to ion migration in a porous electrode.[90] The radius of the semi-circle decreased by nearly a factor of three when comparing the 60 °C and RT case which is commensurate with the expected increase in ionic conductivity as shown by Leys et al.[91] In both cases, at low frequencies, the Nyquist plots rise nearly vertically indicating a nearly ideal capacitive behavior.

So far we have only discussed C_G in terms of the capacitance per mass of single electrode. However, a more practical indicator is to include the mass of the electrolyte which can have a significant impact on the practical device energy density. As shown in **Figure 4**d, we also report the gravimetric capacitance per mass of IL and rGO. The capacitance estimated in this way reaches a maximum at 60% IL of 76 F/(g IL + rGO)

and we also observe a maximum at 60 °C of 114 F/(g IL + rGO). As shown in **Figure 5.3f**, the bulk density of rGO in the electrodes decreases from about 1 g/cm^3 to 0.48 g/cm^3 when the IL content is increased from 20% to 80% which is caused by more IL being during casting. The decreasing bulk density but increasing C_G led to a maximum in C_V at 60% IL (0.76 g/cm^3) of 218 F/cm^3 for the 60 °C case. As will be discussed later, this is the highest volumetric capacitance reported for a graphene-based material in an IL electrolyte due to a combination of high ρ_{bulk} and high C_G which is facilitated by the microemulsion approach developed. To evaluate the prospect of our IM-rGO electrodes for practical application, we also tested the performance of much thicker IM-rGO films with mass loadings up to 4 mg/cm^2 as shown in **Figure 5.3e**. Between 0.75 mg/cm^2 and 1.5 mg/cm^2 the capacitance remains the same but then drops by ~ 23% and ~17 % when a loading of 4 mg/cm^2 at RT and 60 °C, respectively, is used. The small decrease in C_V with loading is partly due to the fact that the bulk density decreases when thicker films (to 0.69 g/cm^3 for 4 mg/cm^2 loading) are cast but the decrease is also influenced by the increased resistance with the increasing electrode thickness.

To better understand the morphology of the films formed at 60% IL, the films were observed by SEM (**Figure 5.4)**. The surface of the films reveal the presence of macropores with uniform diameter of about 20 µm which likely formed by evaporation of water and Tween 20 during thermal treatment. Some of these pores appear to also exist as pockets within the bulk of the film. As shown in **Figure 5.5**, the size of these pores/pockets scales with the IL content (or Tween 20 content as the ratio of IL to Tween 20 was fixed). Analysis of film cross-sections indicates that film forms a layered structure, suggesting that most of the sheets dry in a morphological parallel to the current collector

leading to the relatively high bulk density. However, eliminating these macropores in the future work could lead to even higher bulk density and, correspondingly, higher C_V.

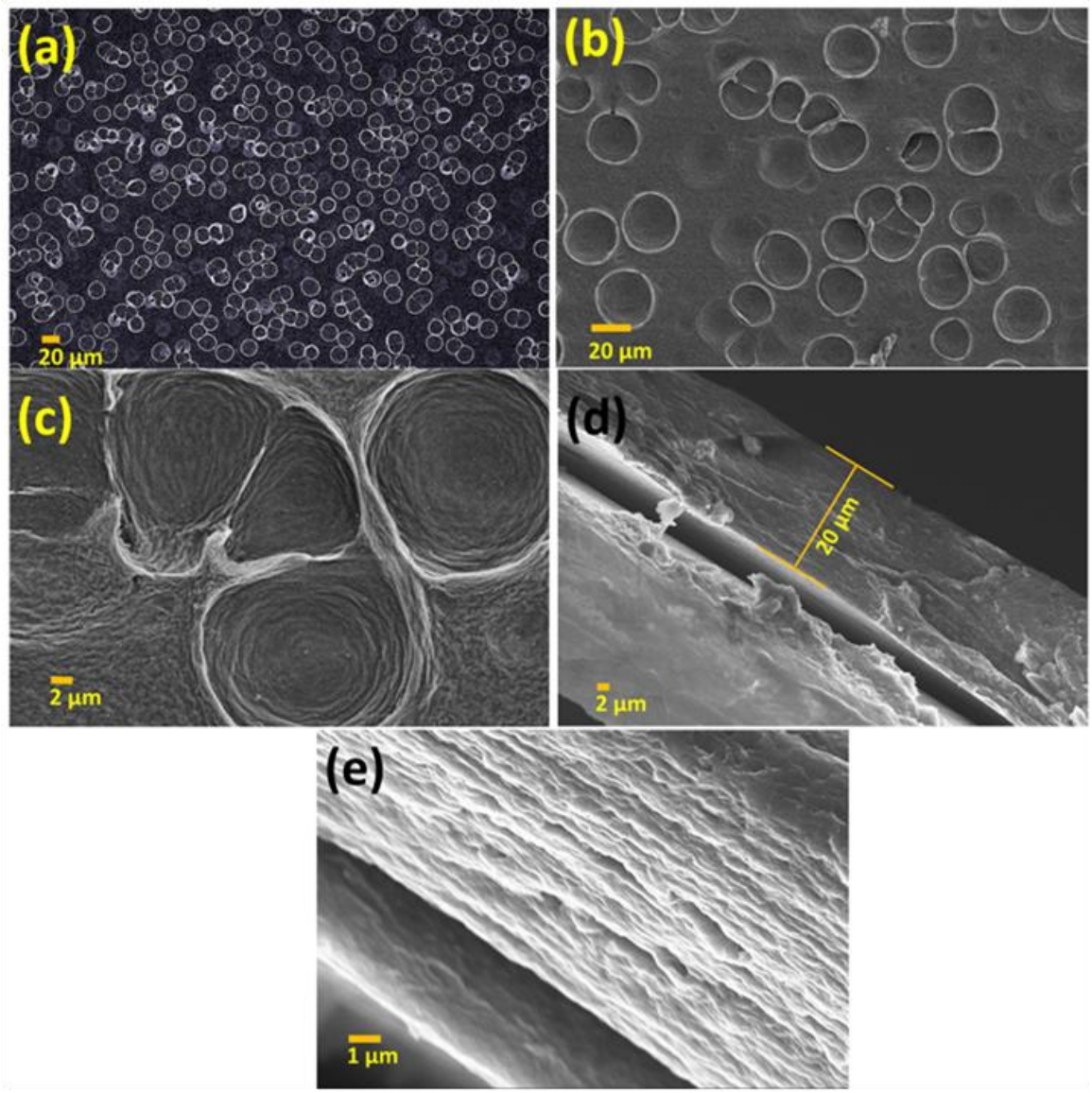

Figure 5.4. Morphology of rGO/IL (60 wt% IL) nanocomposite electrodes determined by SEM. (a, b and c) Surface morphology of the IM-rGO film at different magnifications; (d and e) cross-section images of IM-rGO film at different magnifications.

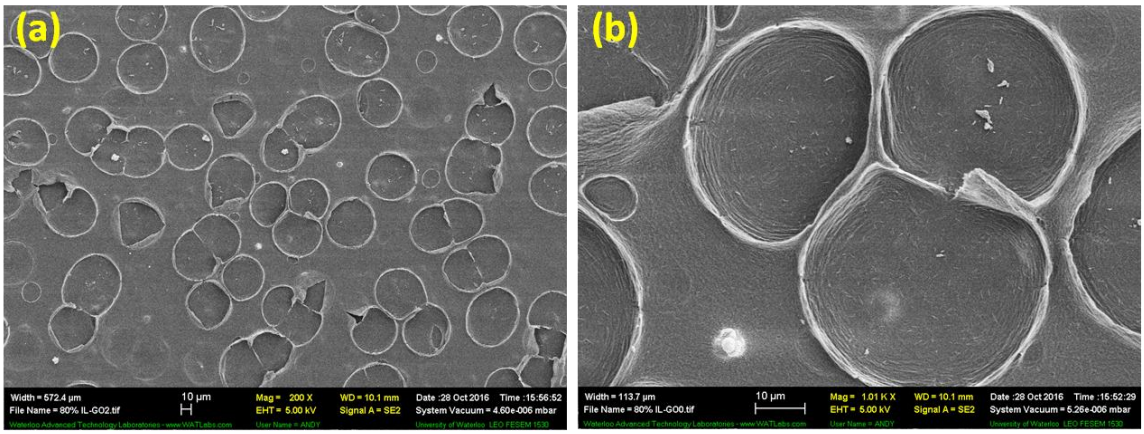

Figure 5.5. (a) and (b) Surface morphology at different magnifications for IM-rGO containing 80 wt% of EMImTFSI.

In an attempt to determine whether the surfactant and microemulsion are necessary for the good electrochemical performance observed, we designed a control experiment where the hydrophobic IL was dissolved in organic solvent, mixed with GO, dried and heat treated in the same way as the microemulsion case. **Figure 5.6** shows CVs for electrodes containing 60% IL at RT prepared without the surfactant or microemulsion system on Cu foil at various scan rates. A maximum capacitance of only 125 F/g at 5 mV/s was found for this case which decreased to 41 F/g at 100 mV/s. This maximum of

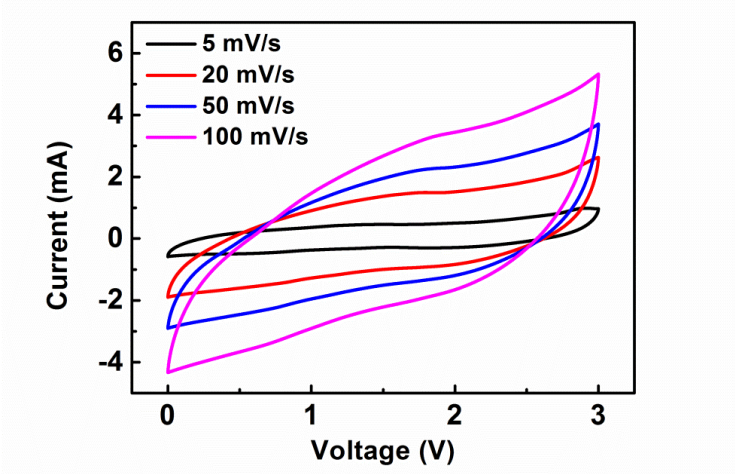

Figure 5.6. The CV plot for the control group without surfactant.

capacitance is similar to what was observed in our previous work where films were cast from aqueous GO/IL gels indicating that casting mixtures of GO and IL without strong specific interactions cannot yield as high performance electrodes as the current method. For comparison, **Figure 5.7a** shows the CV plots of the IM-rGO electrodes (60% IL) at RT at different scan rates. All the CV plots show a nearly rectangular shape indicating the charge storage mechanism is likely non-faradaic in nature, as expected for the aprotic electrolyte system used. The maximum C_G obtained from the CV plot was 186 F/g at 5 mV/s scan rate, which was similar to what was obtained by GCD testing at similar rates (189 F/g at 1 A/g), and retained high C_G of 83 F/g even at high scan rate of 100 mV/s.

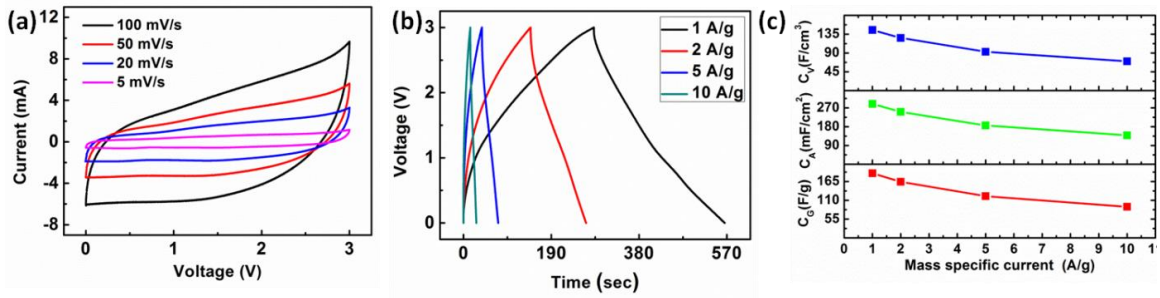

Figure 5.7. Electrochemical performance of 60% IL electrodes at RT. (a) CVs and (b) GCDs for IM-rGO at RT; (c) specific capacitance (RT) at varying current density.

The GCD plots of the IM-rGO electrodes (60% IL, RT) at different mass specific current of 1, 2, 5 and 10 A/g is shown in **Figure 5.7b**. All the GCD plots show almost linear charge-discharge curves with only a small IR drop. All the GCD plots maintained high columbic efficiency of 90% to 95% indicating the reversibility of the system. The C_G, areal capacitance (C_A) and volumetric capacitance (C_V) for the optimal 60% case are shown in **Figure 5.7c** as a function of mass specific current. The maximum values of C_G, C_A and C_V obtained from the GCD plot at 1 A/g current were 189 F/g, 289 mF/cm^2 and 145 F/cm^3, respectively for RT cycling.

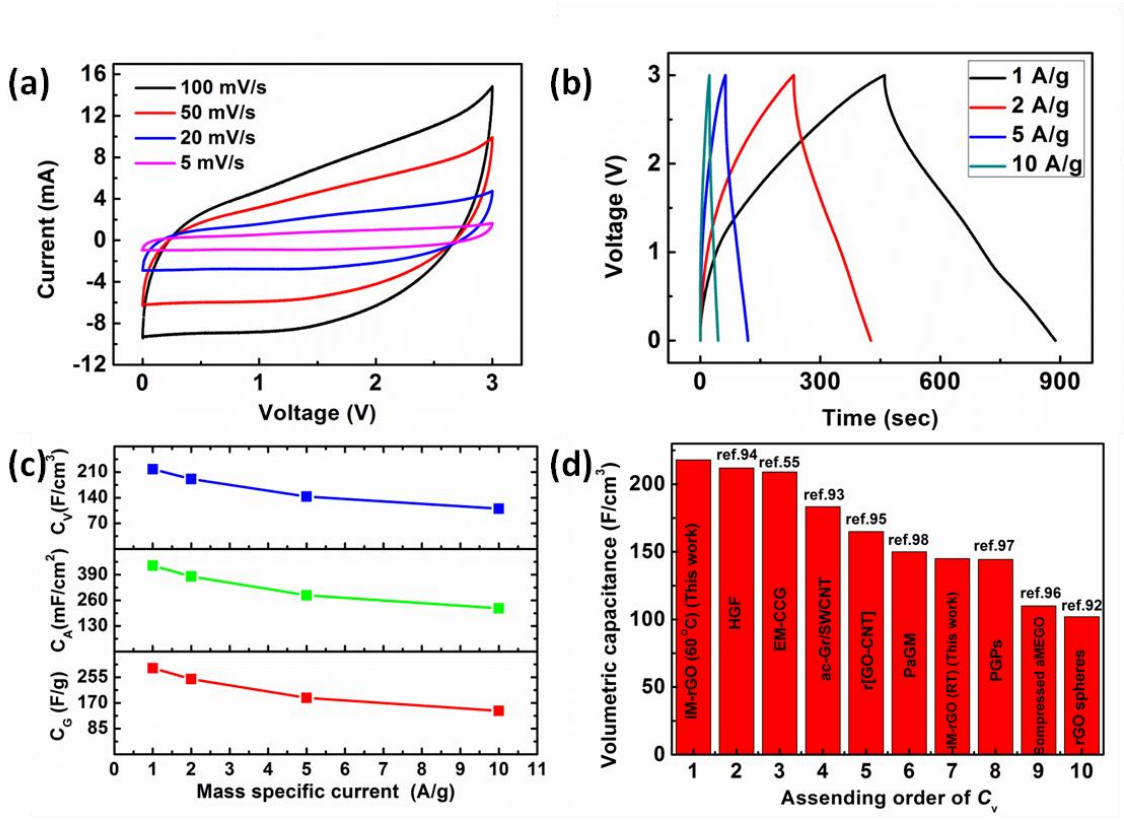

Figure 5.8. Electrochemical performance of 60% IL electrodes at 60 °C. (a) CV and (b) GCD plots for IM-rGO at 60 °C; (c) capacitances (60 °C) at varying current densities; (d) the top 10[55, 92-98] of volumetric capacitance reported recent years for graphene based symmetric supercapacitors.

The electrochemical performance at 60 °C was also investigated in more detail by CV and GCD as shown in **Figure 5.8a and b**, respectively. Like the RT behavior, the CV plots at 60 °C also exhibit nearly rectangular shape but with a higher current response for the same loading of active material and same scan rate. The maximum C_G obtained from the CV plot at 5 mV/s was 282 F/g and retained high C_G of 124 F/g even at a high scan rate of 100 mV/s. The GCD plots at different mass specific current also maintained lineraity with high coulombic efficiency (88% to 93%) at 60 °C with ~1.5 times higher capacitance than RT at 1 A/g current. The variation of C_G, C_A and C_V as a function of current density is shown in **Figure 5.8c**. The maximum C_G and C_A obtained were 285 F/g and 436 mF/cm^2 (965 mF/cm^2 at the mass loading of 4 mg/cm^2) which are amongst the

highest values reported for graphene-based supercapacitors operated in a high voltage-capable IL electrolyte. By virtue of the high packing density (0.76 g/cm^3) of the IM-rGO electrode with 60% IL, the C_V is 218 F/cm^3 at 1 A/g. The elevated temperature increased the ionic mobility and also resulted in improved rate capabilities. In **Figure 5.8d**, the best C_V achieved for the IM-rGO supercapacitor are compared with the top results reported in the literature, to date, for graphene-based materials (under comparable testing conditions). The IM-rGO electrodes fabricated using the IL microemulsion and operated at RT is amongst the highest reported while the performance at 60 °C is the highest reported to date.

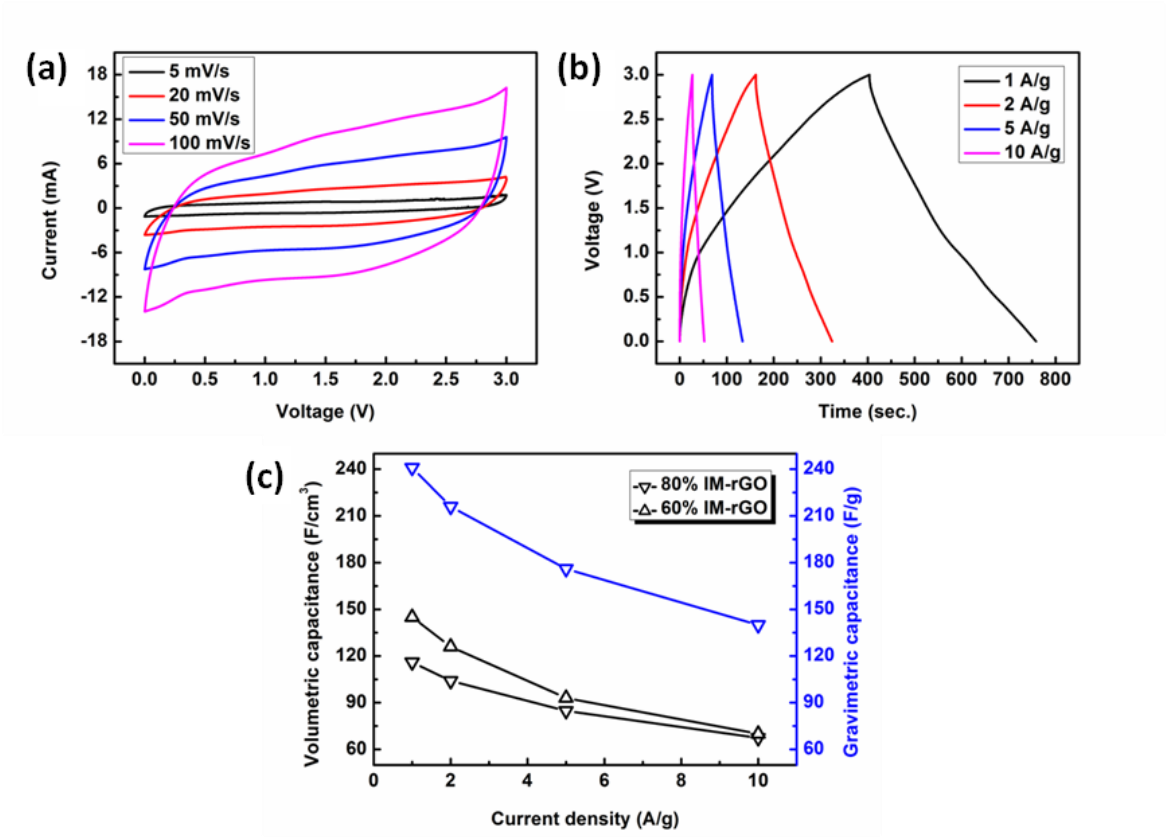

Figure 5.9. (a) CVs and (b) GCDs for IM-rGO containing 80 wt% of EMImTFSI at RT, (c) specific capacitance (RT) at varying current density for IM-rGO with different content of IL.

The electrochemical performance for IM-rGO formed at 80 wt% of IL was also investigated by CV and GCD as shown in **Figure 5.9a and b**, respectively. Like the RT behavior for electrodes containing 60 wt% IL, the CV plots also showed near rectangular behavior but with a higher current response for the same loading of active material and same scan rate. The GCD plots at different mass specific current also maintained its lineraity with high coulombic efficiency, and the corresponding C_G and C_V as a function of current density is shown in **Figure 5.9c**. The maximum C_G obtained was 241 F/g at 1 A/g current and retained as high as 140 F/g even at a high current density of 10 A/g suggesting a better rate ability (58%) than that (48%) of electrodes containg 60 wt% of IL. However, limited by the low packing density (0.48 g/cm^3), the C_V of 80% elecrodes (67.4 F/cm^3) is lower than that of 60 % even at a high current density of 10 A/g.

To understand the long-term cycling ability of the as fabricated IM-rGO electrode the GCD test was continued up to 1000 times at both RT and at 60 °C at 10 A/g current (**Figure 5.10**a). The IM-rGO electrodes retained ~92.1% and ~90.3% of its initial capacitance, respectively at RT and at 60 °C. While the RT cells could achieve beyond 5000 cycles with little decay, the 60 °C ones became unstable due to the harsher conditions. We suspect that the suboptimal cycle-life is related to impurities introduced during the thermal reduction of GO and the evaporation/decomposition of the Tween 20. The complex multicomponent system poses a characterization challenge and these aspects are left to future work.

A Ragone plot indicating the estimated single electrode energy density of the IM-rGO electrode tested at both RT and at 60 °C is shown in **Figure 5.10b** in comparison to recently reported results based on supercapacitors fabricated using graphene and related

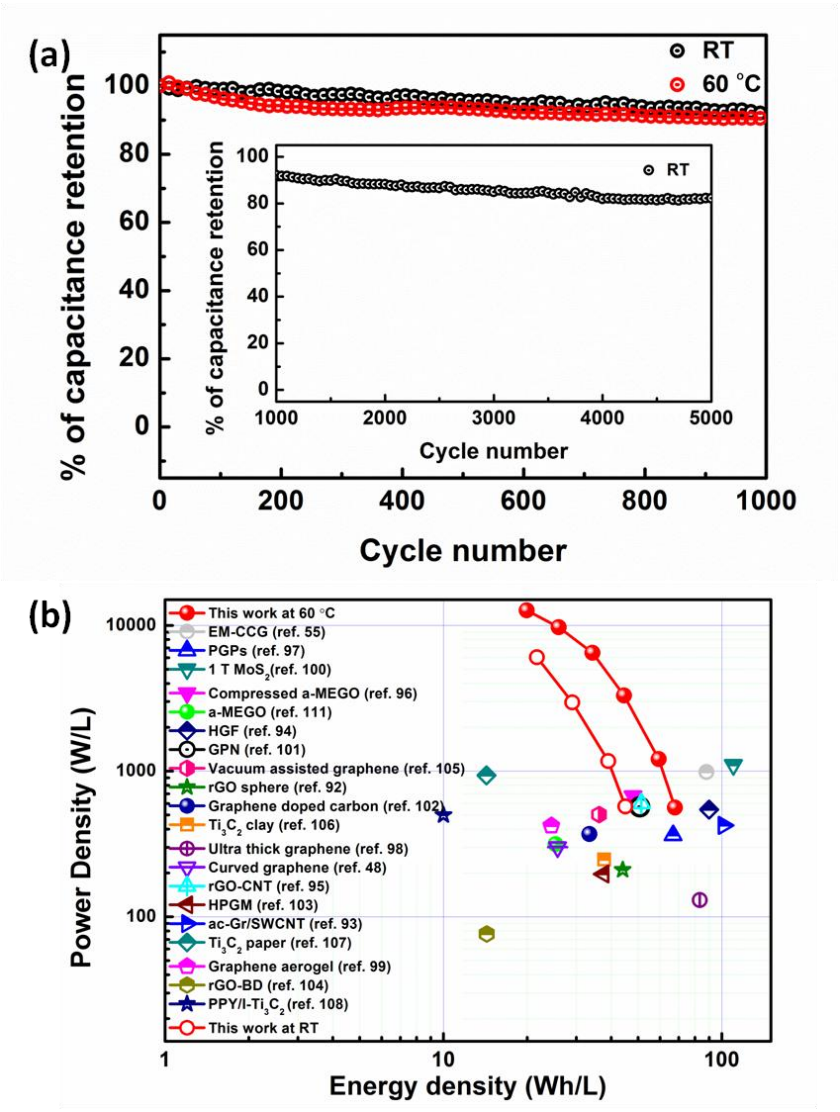

Figure 5.10. (a) Cyclic stability testing at RT and 60 oC; (b) Ragone plots[41, 48, 55, 86, 92-108] of symmetric supercapacitors based on graphene and related 2D materials (MoS2, Mxene).

2D materials (ex. Mxene and molybdenum disulfide). It should be noted that to convert these values to a cell-level energy density, the single electrode density would have to be divided by a factor of four to account for the mass of each electrode and the series configuration of a two electrode cell. Furthermore, one would have to account for the fact that the active material is only ~10-30% of the full cell mass/volume which depends on

the relative mass/thickness of the active material compared to the other cell components (ex. current collectors, membrane separator, packaging).

All literature results of energy densities and power densities were estimated at very close testing condition (~1 A/g current). The IM-rGO electrode exhibits a maximum volumetric energy density of 45 Wh/L at a power density of 571.4 W/L and maintains its high energy density of 21.7 Wh/L at a power density as high as 6.04 kW/L at RT. At 60 °C the IM-rGO electrode exhibits a maximum energy density of 67.8 Wh/L at power density of 561.4 W/L and maintained its energy density of 19.9 Wh/L at a very high power density of 12.69 kW/L.

Compared to other recently published methods on creating energy dense graphene-based supercapacitors, our procedure has several distinct advantages. The GO/IL microemulsion formulations can be easily adapted to conventional casting procedures – making the process amenable to large-scale supercapacitor manufacturing. It also doesn't require chemical reduction or high temperatures, reducing hazardous chemical waste and processing costs. This is in contrast to most other approaches which rely on slow vacuum filtration[55, 92-93, 99-100] and solvent exchange processes[55, 94] which cannot be made roll-to-roll, common chemical or hydrothermal reduction,[55, 94-95, 99-104] chemical/thermal activation[41, 92-93, 95-98, 101-102] and high pressure mechanical compression[94, 96, 98] procedures. Furthermore, our approach eliminates the need to vacuum imbibe the electrolyte into the supercapacitor during cell assembly. This is time consuming and requires specialized high vacuum, liquid handling equipment. In our approach, the electrolyte is cast directly with the electrode material and this step could be completely eliminated.

5.4 Conclusion

In summary, we have demonstrated that graphene oxide dispersions mixed with EMImTFSI/Tween 20/water micro-emulsions cause the spontaneous adsorption of EMImTFSI/Tween 20 to the GO surface. Casting and heat treatment of the resulting films leads to dense rGO electrodes with high IL-accessible SSA. This high SSA leads to the highest C_G reported for graphene-based materials in IL electrolytes of $C_G = 302$ F/g (for 80 wt% IL at 1 A/g) and the high packing density of $\rho_v = 0.76$ g/cm^3 which leads to exceptional volumetric capacitance both at RT and at 60 °C of 144 F/cm^3, and 218 F/cm^3, respectively for films containing 60 wt% IL at 1 A/g. The latter is the highest volumetric capacitance ever reported for graphene based symmetric supercapacitor leading to exceptional energy density of 67.8 Wh/L at power density of 561.4 W/L. Our approach is simple, scalable, and eliminates the electrolyte imbibition step in supercapacitor manufacturing.

6 Conclusions and Future Works

6.1 Summary of Main Conclusions

The work presented in this thesis has contributed to the development and understanding of a new electrode fabrication strategy on thermally reduced graphene oxide sheets. The two main challenges, the spontaneous restacking tendency of reduced graphene oxide sheets and partial ion-accessible surface area, which limit device capacitance, were improved by imbibing electrolyte (a non-volatile ionic liquid) into graphene oxide sheets before reduction acted as both a softer spacer and electrolyte. Based on the above idea presented in our previous work, substituting the former hydrophilic IL by a hydrophobic IL (with better chemical stability and lower viscosity) was explored in Chapter 3. According to the chemical stability test on common and cheap metal current collectors (Al discs, Cu foil), hydrophobic EMImTFSI has better compatibility with copper and aluminum than that of hydrophilic $EMImBF_4$. Due to the difference in thermal behaviour between two ILs, the optimized heat treatment is studied as well with regard to three main parameters, including temperature range, ramp rate and cooling method. The resulting thermally reduced films display the best performance when a balance between sufficient thermal reduction (requiring high temperature) and the reduced loss of IL through evaporation and thermal decomposition. Insufficient reduction

could cause poor conductivity, while significant loss of IL results in cracked films and loss of IL-accessible surface area. Ramping from room temperature to 360 ºC is demonstrated to be the optimal setting and exhibited a gravimetric capacitance of 135 F/g when assembled with 80 wt% of IL. However, this method does not take advantage of any specific attraction between GO and IL, which leads to the partially wetted film after reduction and allows us to reach only a small fraction of the theoretically predicted capacitance (400-500 F/g). In an analogy with the concept of drug delivery, surfactant micelles are regarded as the "capsule" here to load and protect hydrophobic IL in order that they may disperse uniformly in water. This system is a so-called microemulsion which is thermodynamically stable, leading to a stable and optically clear dispersion with a narrow size distribution (~8 nm). These microemulsion nanodroplets are subsequently identified as being capable of spontaneously adsorbing onto the surface of GO sheets driven by hydrogen bonding. This self-assembly behavior is used to fabricate dense and uniform IL/rGO electrodes following room temperature evaporation (water removal) and thermal reduction (removal of the surfactant and restoring the conductivity of graphene). Such an approach effectively limits the thermal expansion and leads to a dense film (0.76 g/cm^3) and boosted volumetric capacitance (218 F/cm^3) standing at the top among all graphene based symmetric capacitance. The enhanced gravimetric capacitance (302 F/g) proves that the IL-accessible surface area is much higher using this approach compared to co-assembly in the absence of any specific interactions.

6.2 Future Directions

6.2.1 Self-assembly Strategy for other 2D Materials

The similar self-assembly technology can be used for other 2D materials as well, such as graphene and MoS_2. It has been proven that substances containing aromatic rings have a highly affinity for carbon nanomaterials,[109] where the strength of the π–π interaction was suggested to depend on size, number and shape of aromatic units. Since graphene is considered to be composed of thousands of aromatic carbon moieties, there is huge potential to achieve the spontaneous adsorption through π–π interaction between graphene sheets and microemulsion nanodroplets if we use the surfactant containing aromatic rings. As for MoS_2, microemulsion nanodroplets could act as both a soft spacer and electrolyte vehicle through an analogous mechanism by adjusting the chemical composition of the surfactant.

6.2.2 Spray Drying and Casting

Spray drying is a method of producing a dry powder with consistent particle size from a liquid or slurry by rapidly drying with a hot gas.[110] This is the preferred method to dry many thermally-sensitive materials such as GO. It has been proven that converting flat graphene oxide sheets to crumpled ball-like morphology can prevent these sheets from restacking through the aggregation-resistance and meanwhile significantly improve the scalabilty of graphene-based supercapacitors by Luo et al.[111] This method could also be combined with the self-assembly strategy described in this paper by a lab mini spray dryer so as to achieve scalable production. After the heat treatment at a proper temperature to reduce GO and remove surfactant, the resulting dry powder could enable the improvement of packing density upon creating compressed electrodes. Furthermore,

spray dried power could be mixed with compatible binder in some solvent to form ink used for screen printing or spray coating on any commercial current collector.

6.2.3 Enhancement of IM-rGO Cyclic Stability

Apart from extending this self-assembly technology to other materials or electrodes farbrication methods, enhancing the suboptimal cyclic stability is also an important task in future work. As we described in Chapter 5, IM-rGO can only stably cycle 5000 times and 1000 times at room temperature and 60 ºC respectively, which are lower than some to relevant works (typically >10000 cycles). We ascribe this to impurities introduced during the thermal reduction of GO and the evaporation/decomposition of the Tween 20. Since every component is thermally stable when they exist individually, there must be some temperature-related reaction that has occurred between them. Through a series of variable control experiments, we can find where the problem is and figure out corresponding resolution to improve device cycle life.

References

1. Pumera, M., Graphene-based nanomaterials for energy storage. *Energy & Environmental Science* **2011,** *4* (3), 668-674.

2. Conway, B. E., *Electrochemical supercapacitors: scientific fundamentals and technological applications*. Springer Science & Business Media: 2013.

3. Zhang, L. L.; Zhao, X., Carbon-based materials as supercapacitor electrodes. *Chemical Society Reviews* **2009,** *38* (9), 2520-2531.

4. 2012Petroleum, B., BP statistical review of world energy. London: British Petroleum: 2012.

5. 2004Winter, M.; Brodd, R. J., What are batteries, fuel cells, and supercapacitors? ACS Publications: 2004.

6. Burke, A., Ultracapacitors: why, how, and where is the technology. *Journal of power sources* **2000,** *91* (1), 37-50.

7. Khaligh, A.; Li, Z., Battery, ultracapacitor, fuel cell, and hybrid energy storage systems for electric, hybrid electric, fuel cell, and plug-in hybrid electric vehicles: State of the art. *IEEE transactions on Vehicular Technology* **2010,** *59* (6), 2806-2814.

8. Zhang, Y.; Feng, H.; Wu, X.; Wang, L.; Zhang, A.; Xia, T.; Dong, H.; Li, X.; Zhang, L., Progress of electrochemical capacitor electrode materials: A review. *International journal of hydrogen energy* **2009,** *34* (11), 4889-4899.

9. Simon, P.; Gogotsi, Y., Capacitive energy storage in nanostructured carbon–electrolyte systems. *Accounts of chemical research* **2012,** *46* (5), 1094-1103.

10. Gouy, G., Phys. 9, 457 (1910). *Ann. Phys.(Paris)* **1917,** *7*, 163.

11. Fowler, R. H.; Guggenheim, E. A., Statistical thermodynamics. **1941**.

12. Beck, F.; Dolata, M.; Grivei, E.; Probst, N., Electrochemical supercapacitors based on industrial carbon blacks in aqueous H2SO4. *Journal of applied electrochemistry* **2001,** *31* (8), 845-853.

13. Du, X.; Wang, C.; Chen, M.; Jiao, Y.; Wang, J., Electrochemical performances of nanoparticle Fe3O4/activated carbon supercapacitor using KOH electrolyte solution. *The Journal of Physical Chemistry C* **2009,** *113* (6), 2643-2646.

14. Béguin, F.; Presser, V.; Balducci, A.; Frackowiak, E., Carbons and electrolytes for advanced supercapacitors. *Advanced materials* **2014,** *26* (14), 2219-2251.

15. Naguib, M.; Mochalin, V. N.; Barsoum, M. W.; Gogotsi, Y., 25th anniversary article: MXenes: a new family of two-dimensional materials. *Advanced Materials* **2014,** *26* (7), 992-1005.

16. Khomenko, V.; Raymundo-Pinero, E.; Béguin, F., Optimisation of an asymmetric manganese oxide/activated carbon capacitor working at 2V in aqueous medium. *Journal of Power Sources* **2006,** *153* (1), 183-190.

17. Chmiola, J.; Gogotsi, Y., Supercapacitors as advanced energy storage devices. *Nanotech. L. & Bus.* **2007,** *4*, 11.

18. Zheng, J.; Cygan, P.; Jow, T., Hydrous ruthenium oxide as an electrode material for electrochemical capacitors. *Journal of the Electrochemical Society* **1995,** *142* (8), 2699-2703.

19. Lee, H.; Cho, M. S.; Kim, I. H.; Do Nam, J.; Lee, Y., RuOx/polypyrrole nanocomposite electrode for electrochemical capacitors. *Synthetic Metals* **2010,** *160* (9), 1055-1059.

20. Augustyn, V.; Simon, P.; Dunn, B., Pseudocapacitive oxide materials for high-rate electrochemical energy storage. *Energy & Environmental Science* **2014,** *7* (5), 1597-1614.

21. Frackowiak, E., Carbon materials for supercapacitor application. *Physical chemistry chemical physics* **2007,** *9* (15), 1774-1785.

22. Li, W.-C.; Nong, G.-Z.; Lu, A.-H.; Hu, H.-Q., Synthesis of nanocast ordered mesoporous carbons and their application as electrode materials for supercapacitor. *Journal of Porous Materials* **2011,** *18* (1), 23-30.

23. Wei, W.; Cui, X.; Chen, W.; Ivey, D. G., Manganese oxide-based materials as electrochemical supercapacitor electrodes. *Chemical society reviews* **2011,** *40* (3), 1697-1721.

24. Mimani, T.; Patil, K., Solution combustion synthesis of nanoscale oxides and their composites. *Materials Physics and Mechanics(Russia)* **2001,** *4* (2), 134-137.

25. Yuan, C.; Zhang, X.; Su, L.; Gao, B.; Shen, L., Facile synthesis and self-assembly of hierarchical porous NiO nano/micro spherical superstructures for high performance supercapacitors. *Journal of Materials Chemistry* **2009,** *19* (32), 5772-5777.

26. Wu, Z. S.; Wang, D. W.; Ren, W.; Zhao, J.; Zhou, G.; Li, F.; Cheng, H. M., Anchoring hydrous RuO2 on graphene sheets for high-performance electrochemical capacitors. *Advanced Functional Materials* **2010,** *20* (20), 3595-3602.

27. Sathiya, M.; Prakash, A.; Ramesha, K.; Tarascon, J. M.; Shukla, A., V2O5-anchored carbon nanotubes for enhanced electrochemical energy storage. *Journal of the American Chemical Society* **2011,** *133* (40), 16291-16299.

28. Yu, G.; Hu, L.; Vosgueritchian, M.; Wang, H.; Xie, X.; McDonough, J. R.; Cui, X.; Cui, Y.; Bao, Z., Solution-processed graphene/MnO2 nanostructured textiles for high-performance electrochemical capacitors. *Nano letters* **2011,** *11* (7), 2905-2911.

29. Snook, G. A.; Kao, P.; Best, A. S., Conducting-polymer-based supercapacitor devices and electrodes. *Journal of Power Sources* **2011,** *196* (1), 1-12.

30. Frackowiak, E.; Khomenko, V.; Jurewicz, K.; Lota, K.; Béguin, F., Supercapacitors based on conducting polymers/nanotubes composites. *Journal of Power Sources* **2006,** *153* (2), 413-418.

31. Li, H.; Wang, J.; Chu, Q.; Wang, Z.; Zhang, F.; Wang, S., Theoretical and experimental specific capacitance of polyaniline in sulfuric acid. *Journal of Power Sources* **2009,** *190* (2), 578-586.

32. Zhang, K.; Zhang, L. L.; Zhao, X.; Wu, J., Graphene/polyaniline nanofiber composites as supercapacitor electrodes. *Chemistry of Materials* **2010,** *22* (4), 1392-1401.

33. Wang, G.; Tang, Q.; Bao, H.; Li, X.; Wang, G., Synthesis of hierarchical sulfonated graphene/MnO 2/polyaniline ternary composite and its improved electrochemical performance. *Journal of Power Sources* **2013,** *241*, 231-238.

34. Novoselov, K. S.; Geim, A. K.; Morozov, S. V.; Jiang, D.; Zhang, Y.; Dubonos, S. V.; Grigorieva, I. V.; Firsov, A. A., Electric field effect in atomically thin carbon films. *science* **2004,** *306* (5696), 666-669.

35. Lee, C.; Wei, X.; Kysar, J. W.; Hone, J., Measurement of the elastic properties and intrinsic strength of monolayer graphene. *science* **2008,** *321* (5887), 385-388.

36. Stoller, M. D.; Park, S.; Zhu, Y.; An, J.; Ruoff, R. S., Graphene-based ultracapacitors. *Nano letters* **2008,** *8* (10), 3498-3502.

37. Bolotin, K. I.; Sikes, K.; Jiang, Z.; Klima, M.; Fudenberg, G.; Hone, J.; Kim, P.; Stormer, H., Ultrahigh electron mobility in suspended graphene. *Solid State Communications* **2008,** *146* (9), 351-355.

38. Pope, M. A.; Aksay, I. A., Four-Fold Increase in the Intrinsic Capacitance of Graphene through Functionalization and Lattice Disorder. *The Journal of Physical Chemistry C* **2015,** *119* (35), 20369-20378.

39. Dreyer, D. R.; Park, S.; Bielawski, C. W.; Ruoff, R. S., The chemistry of graphene oxide. *Chemical Society Reviews* **2010,** *39* (1), 228-240.

40. Gómez-Navarro, C.; Weitz, R. T.; Bittner, A. M.; Scolari, M.; Mews, A.; Burghard, M.; Kern, K., Electronic transport properties of individual chemically reduced graphene oxide sheets. *Nano letters* **2007,** *7* (11), 3499-3503.

41. Zhu, Y.; Murali, S.; Stoller, M. D.; Ganesh, K.; Cai, W.; Ferreira, P. J.; Pirkle, A.; Wallace, R. M.; Cychosz, K. A.; Thommes, M., Carbon-based supercapacitors produced by activation of graphene. *Science* **2011,** *332* (6037), 1537-1541.

42. Si, Y.; Samulski, E. T., Exfoliated graphene separated by platinum nanoparticles. *Chemistry of Materials* **2008,** *20* (21), 6792-6797.

43. Yan, J.; Wei, T.; Shao, B.; Ma, F.; Fan, Z.; Zhang, M.; Zheng, C.; Shang, Y.; Qian, W.; Wei, F., Electrochemical properties of graphene nanosheet/carbon black composites as electrodes for supercapacitors. *Carbon* **2010,** *48* (6), 1731-1737.

44. Wang, H.; Hao, Q.; Yang, X.; Lu, L.; Wang, X., Graphene oxide doped polyaniline for supercapacitors. *Electrochemistry Communications* **2009,** *11* (6), 1158-1161.

45. Balducci, A.; Bardi, U.; Caporali, S.; Mastragostino, M.; Soavi, F., Ionic liquids for hybrid supercapacitors. *Electrochemistry communications* **2004,** *6* (6), 566-570.

46. Kim, T. Y.; Lee, H. W.; Stoller, M.; Dreyer, D. R.; Bielawski, C. W.; Ruoff, R. S.; Suh, K. S., High-performance supercapacitors based on poly (ionic liquid)-modified graphene electrodes. *ACS nano* **2010,** *5* (1), 436-442.

47. Vivekchand, S.; Rout, C. S.; Subrahmanyam, K.; Govindaraj, A.; Rao, C., Graphene-based electrochemical supercapacitors. *Journal of Chemical Sciences* **2008,** *120* (1), 9-13.

48. Liu, C.; Yu, Z.; Neff, D.; Zhamu, A.; Jang, B. Z., Graphene-based supercapacitor with an ultrahigh energy density. *Nano letters* **2010,** *10* (12), 4863-4868.

49. Pope, M. A.; Korkut, S.; Punckt, C.; Aksay, I. A., Supercapacitor electrodes produced through evaporative consolidation of graphene oxide-water-ionic liquid gels. *Journal of The Electrochemical Society* **2013,** *160* (10), A1653-A1660.

50. Mousavi, M. P.; Wilson, B. E.; Kashefolgheta, S.; Anderson, E. L.; He, S.; Bühlmann, P.; Stein, A., Ionic Liquids as Electrolytes for Electrochemical Double-Layer Capacitors: Structures that Optimize Specific Energy. *ACS applied materials & interfaces* **2016,** *8* (5), 3396-3406.

51. Balducci, A.; Dugas, R.; Taberna, P.-L.; Simon, P.; Plee, D.; Mastragostino, M.; Passerini, S., High temperature carbon–carbon supercapacitor using ionic liquid as electrolyte. *Journal of Power Sources* **2007,** *165* (2), 922-927.

52. Bozym, D. J.; Uralcan, B. l.; Limmer, D. T.; Pope, M. A.; Szamreta, N. J.; Debenedetti, P. G.; Aksay, I. A., Anomalous capacitance maximum of the glassy

carbon–ionic liquid interface through dilution with organic solvents. *The journal of physical chemistry letters* **2015,** *6* (13), 2644-2648.

53. Dagousset, L.; Nguyen, G. T.; Vidal, F.; Galindo, C.; Aubert, P.-H., Ionic liquids and γ-butyrolactone mixtures as electrolytes for supercapacitors operating over extended temperature ranges. *RSC Advances* **2015,** *5* (17), 13095-13101.

54. Bozym, D. J.; Korkut, S.; Pope, M. A.; Aksay, I. A., Dehydrated Sucrose Nanoparticles as Spacers for Graphene–Ionic Liquid Supercapacitor Electrodes. *ACS Sustainable Chemistry & Engineering* **2016,** *4* (12), 7167-7174.

55. Yang, X.; Cheng, C.; Wang, Y.; Qiu, L.; Li, D., Liquid-mediated dense integration of graphene materials for compact capacitive energy storage. *science* **2013,** *341* (6145), 534-537.

56. Russel, W. B.; Saville, D. A.; Schowalter, W. R., *Colloidal dispersions*. Cambridge university press: 1989.

57. Zhang, Z.; Gao, X.; Yang, L., Electrochemical properties of room temperature ionic liquids incorporating BF4− and TFSI− anions as green electrolytes. *Chinese science bulletin* **2005,** *50* (18).

58. Liu, S.-Q.; Zhang, K.; Yuen, M. M.; Fu, X.-Z.; Sun, R.; Wong, C.-P. In *Effect of reduction temperatures on the thermal and electrical conductivities of reduced graphene oxide films on the Cu foils*, Electronic Packaging Technology (ICEPT), 2016 17th International Conference on, IEEE: 2016; pp 310-312.

59. Huh, S. H., Thermal reduction of graphene oxide. In *Physics and Applications of Graphene-Experiments*, InTech: 2011.

60. Hoar, T.; Schulman, J., Transparent water-in-oil dispersions: the oleopathic hydro-micelle. *Nature* **1943,** *152* (3847), 102-103.

61. Schulman, J. H.; Stoeckenius, W.; Prince, L. M., Mechanism of formation and structure of micro emulsions by electron microscopy. *The Journal of physical chemistry* **1959,** *63* (10), 1677-1680.

62. Jadhav, K.; Shaikh, I.; Ambade, K.; Kadam, V., Applications of microemulsion based drug delivery system. *Current drug delivery* **2006,** *3* (3), 267-273.

63. Howard, J.; Hadgraft, J., The clearance of oily vehicles following intramuscular and subcutaneous injections in rabbits. *International Journal of Pharmaceutics* **1983,** *16* (1), 31-39.

64. Gao, Y. a.; Li, N.; Zheng, L.; Zhao, X.; Zhang, S.; Han, B.; Hou, W.; Li, G., A cyclic voltammetric technique for the detection of micro-regions of bmimPF6/Tween 20/H 2 O microemulsions and their performance characterization by UV-Vis spectroscopy. *Green Chemistry* **2006,** *8* (1), 43-49.

65. Gillberg, G.; Lehtinen, H.; Friberg, S., NMR and IR investigation of the conditions determining the stability of microemulsions. *Journal of Colloid and Interface Science* **1970,** *33* (1), 40-53.

66. Paul, B. K.; Moulik, S. P., Microemulsions: an overview. *Journal of Dispersion science and Technology* **1997,** *18* (4), 301-367.

67. Chokshi, K.; Qutubuddin, S.; Hussam, A., Electrochemical investigation of microemulsions. *Journal of colloid and interface science* **1989,** *129* (2), 315-326.

68. Mackay, R. A.; Myers, S. A.; Bodalbhai, L.; Brajter-Toth, A., Microemulsion structure and its effect on electrochemical reactions. *Analytical chemistry* **1990,** *62* (10), 1084-1090.

69. Ip, A. C. F.; Liu, B.; Huang, P. J. J.; Liu, J., Oxidation Level-Dependent Zwitterionic Liposome Adsorption and Rupture by Graphene-based Materials and Light-Induced Content Release. *Small* **2013,** *9* (7), 1030-1035.

70. Kagan, M. R.; McCreery, R. L., Reduction of fluorescence interference in Raman spectroscopy via analyte adsorption on graphitic carbon. *ANALYTICAL CHEMISTRY-WASHINGTON DC-* **1994,** *66*, 4159-4159.

71. Kubin, R. F.; Fletcher, A. N., Fluorescence quantum yields of some rhodamine dyes. *Journal of Luminescence* **1982,** *27* (4), 455-462.

72. Hu, Y.; Li, Z.; Li, H.; Liu, Y.; Song, S., Roles of hydrocarbon chain-length in preparing graphene oxide from mildly-oxidized graphite with intercalating anionic aliphatic surfactants. *RSC Advances* **2016,** *6* (18), 14859-14867.

73. Medhekar, N. V.; Ramasubramaniam, A.; Ruoff, R. S.; Shenoy, V. B., Hydrogen bond networks in graphene oxide composite paper: structure and mechanical properties. *Acs Nano* **2010,** *4* (4), 2300-2306.

74. Miller, J. R.; Simon, P., Electrochemical capacitors for energy management. *Science Magazine* **2008,** *321* (5889), 651-652.

75. Simon, P.; Gogotsi, Y., Materials for electrochemical capacitors. *Nature materials* **2008,** *7* (11), 845-854.

76. Du Pasquier, A.; Plitz, I.; Menocal, S.; Amatucci, G., A comparative study of Li-ion battery, supercapacitor and nonaqueous asymmetric hybrid devices for automotive applications. *Journal of Power Sources* **2003,** *115* (1), 171-178.

77. Burke, A., R&D considerations for the performance and application of electrochemical capacitors. *Electrochimica Acta* **2007,** *53* (3), 1083-1091.

78. Linden, D. In *Handbook of batteries*, Fuel and Energy Abstracts, 1995; p 265.

79. Wang, Y.; Chen, J.; Cao, J.; Liu, Y.; Zhou, Y.; Ouyang, J.-H.; Jia, D., Graphene/carbon black hybrid film for flexible and high rate performance supercapacitor. *Journal of Power Sources* **2014,** *271*, 269-277.

80. Zheng, Q.; Zhang, B.; Lin, X.; Shen, X.; Yousefi, N.; Huang, Z.-D.; Li, Z.; Kim, J.-K., Highly transparent and conducting ultralarge graphene oxide/single-walled carbon nanotube hybrid films produced by Langmuir–Blodgett assembly. *Journal of Materials Chemistry* **2012,** *22* (48), 25072-25082.

81. Cheng, C.; Li, D., Solvated graphenes: an emerging class of functional soft materials. *Advanced Materials* **2013,** *25* (1), 13-30.

82. Yang, X.; Zhu, J.; Qiu, L.; Li, D., Bioinspired effective prevention of restacking in multilayered graphene films: towards the next generation of high-performance supercapacitors. *Advanced Materials* **2011,** *23* (25), 2833-2838.

83. Chen, H.; Müller, M. B.; Gilmore, K. J.; Wallace, G. G.; Li, D., Mechanically strong, electrically conductive, and biocompatible graphene paper. *Advanced Materials* **2008,** *20* (18), 3557-3561.

84. Li, D.; Müller, M. B.; Gilje, S.; Kaner, R. B.; Wallace, G. G., Processable aqueous dispersions of graphene nanosheets. *Nature nanotechnology* **2008,** *3* (2), 101-105.

85. Eda, G.; Fanchini, G.; Chhowalla, M., Large-area ultrathin films of reduced graphene oxide as a transparent and flexible electronic material. *Nature nanotechnology* **2008,** *3* (5), 270-274.

86. Schniepp, H. C.; Li, J.-L.; McAllister, M. J.; Sai, H.; Herrera-Alonso, M.; Adamson, D. H.; Prud'homme, R. K.; Car, R.; Saville, D. A.; Aksay, I. A., Functionalized single graphene sheets derived from splitting graphite oxide. *The Journal of Physical Chemistry B* **2006,** *110* (17), 8535-8539.

87. Acik, M.; Lee, G.; Mattevi, C.; Chhowalla, M.; Cho, K.; Chabal, Y., Unusual infrared-absorption mechanism in thermally reduced graphene oxide. *Nature materials* **2010,** *9* (10), 840-845.

88. Arulepp, M.; Permann, L.; Leis, J.; Perkson, A.; Rumma, K.; Jänes, A.; Lust, E., Influence of the solvent properties on the characteristics of a double layer capacitor. *Journal of Power Sources* **2004,** *133* (2), 320-328.

89. Ervin, M. H.; Levine, L. B.; Nichols, B. M.; Parker, T. C., Thermal processing for graphene oxide supercapacitor electrode reduction and wetting. *Journal of Applied Electrochemistry* **2016,** *46* (10), 1075-1084.

90. Meyers, J. P.; Doyle, M.; Darling, R. M.; Newman, J., The impedance response of a porous electrode composed of intercalation particles. *Journal of The Electrochemical Society* **2000,** *147* (8), 2930-2940.

91. Leys, J.; Wübbenhorst, M.; Preethy Menon, C.; Rajesh, R.; Thoen, J.; Glorieux, C.; Nockemann, P.; Thijs, B.; Binnemans, K.; Longuemart, S., Temperature dependence of the electrical conductivity of imidazolium ionic liquids. *The Journal of chemical physics* **2008,** *128* (6), 064509.

92. Kim, T.; Jung, G.; Yoo, S.; Suh, K. S.; Ruoff, R. S., Activated graphene-based carbons as supercapacitor electrodes with macro-and mesopores. *Acs Nano* **2013,** *7* (8), 6899-6905.

93. Pham, D. T.; Lee, T. H.; Luong, D. H.; Yao, F.; Ghosh, A.; Le, V. T.; Kim, T. H.; Li, B.; Chang, J.; Lee, Y. H., Carbon nanotube-bridged graphene 3D building blocks for ultrafast compact supercapacitors. *ACS nano* **2015,** *9* (2), 2018-2027.

94. Xu, Y.; Lin, Z.; Zhong, X.; Huang, X.; Weiss, N. O.; Huang, Y.; Duan, X., Holey graphene frameworks for highly efficient capacitive energy storage. *Nature communications* **2014,** *5*.

95. Jung, N.; Kwon, S.; Lee, D.; Yoon, D. M.; Park, Y. M.; Benayad, A.; Choi, J. Y.; Park, J. S., Synthesis of chemically bonded graphene/carbon nanotube composites and their application in large volumetric capacitance supercapacitors. *Advanced Materials* **2013,** *25* (47), 6854-6858.

96. Murali, S.; Quarles, N.; Zhang, L. L.; Potts, J. R.; Tan, Z.; Lu, Y.; Zhu, Y.; Ruoff, R. S., Volumetric capacitance of compressed activated microwave-expanded graphite oxide (a-MEGO) electrodes. *Nano Energy* **2013,** *2* (5), 764-768.

97. Li, H.; Tao, Y.; Zheng, X.; Li, Z.; Liu, D.; Xu, Z.; Luo, C.; Luo, J.; Kang, F.; Yang, Q.-H., Compressed porous graphene particles for use as supercapacitor electrodes with excellent volumetric performance. *Nanoscale* **2015,** *7* (44), 18459-18463.

98. Li, H.; Tao, Y.; Zheng, X.; Luo, J.; Kang, F.; Cheng, H.-M.; Yang, Q.-H., Ultra-thick graphene bulk supercapacitor electrodes for compact energy storage. *Energy & Environmental Science* **2016,** *9* (10), 3135-3142.

99. Wang, X.; Lu, C.; Peng, H.; Zhang, X.; Wang, Z.; Wang, G., Efficiently dense hierarchical graphene based aerogel electrode for supercapacitors. *Journal of Power Sources* **2016,** *324*, 188-198.

100. Acerce, M.; Voiry, D.; Chhowalla, M., Metallic 1T phase MoS2 nanosheets as supercapacitor electrode materials. *Nature nanotechnology* **2015,** *10* (4), 313-318.

101. Zhang, H.; Wang, K.; Zhang, X.; Lin, H.; Sun, X.; Li, C.; Ma, Y., Self-generating graphene and porous nanocarbon composites for capacitive energy storage. *Journal of Materials Chemistry A* **2015,** *3* (21), 11277-11286.

102. Yang, X.; Zhang, L.; Zhang, F.; Zhang, T.; Huang, Y.; Chen, Y., A high-performance all-solid-state supercapacitor with graphene-doped carbon material

electrodes and a graphene oxide-doped ion gel electrolyte. *Carbon* **2014,** *72*, 381-386.

103. Tao, Y.; Xie, X.; Lv, W.; Tang, D.-M.; Kong, D.; Huang, Z.; Nishihara, H.; Ishii, T.; Li, B.; Golberg, D., Towards ultrahigh volumetric capacitance: graphene derived highly dense but porous carbons for supercapacitors. *Scientific reports* **2013,** *3*, 2975.

104. Lee, K.; Yoon, Y.; Cho, Y.; Lee, S. M.; Shin, Y.; Lee, H.; Lee, H., Tunable Sub-nanopores of Graphene Flake Interlayers with Conductive Molecular Linkers for Supercapacitors. *ACS nano* **2016,** *10* (7), 6799-6807.

105. Yang, H.; Kannappan, S.; Pandian, A. S.; Jang, J.-H.; Lee, Y. S.; Lu, W., Nanoporous graphene materials by low-temperature vacuum-assisted thermal process for electrochemical energy storage. *Journal of Power Sources* **2015,** *284*, 146-153.

106. Ghidiu, M.; Lukatskaya, M. R.; Zhao, M.-Q.; Gogotsi, Y.; Barsoum, M. W., Conductive two-dimensional titanium carbide/clay/'with high volumetric capacitance. *Nature* **2014,** *516* (7529), 78-81.

107. Lukatskaya, M. R.; Mashtalir, O.; Ren, C. E.; Dall'Agnese, Y.; Rozier, P.; Taberna, P. L.; Naguib, M.; Simon, P.; Barsoum, M. W.; Gogotsi, Y., Cation intercalation and high volumetric capacitance of two-dimensional titanium carbide. *Science* **2013,** *341* (6153), 1502-1505.

108. Zhu, M.; Huang, Y.; Deng, Q.; Zhou, J.; Pei, Z.; Xue, Q.; Huang, Y.; Wang, Z.; Li, H.; Huang, Q., Highly Flexible, Freestanding Supercapacitor Electrode with Enhanced Performance Obtained by Hybridizing Polypyrrole Chains with MXene. *Advanced Energy Materials* **2016,** *6* (21).

109. Mohamed, A.; Ardyani, T.; Bakar, S. A.; Brown, P.; Hollamby, M.; Sagisaka, M.; Eastoe, J., Graphene-philic surfactants for nanocomposites in latex technology. *Advances in colloid and interface science* **2016,** *230*, 54-69.

110. Mujumdar, A. S., *Handbook of industrial drying*. CRC press: 2014.

111. Luo, J.; Jang, H. D.; Huang, J., Effect of sheet morphology on the scalability of graphene-based ultracapacitors. *Acs Nano* **2013,** *7* (2), 1464-1471.